ELECTRON AND METASTABLE DENSITY MEASUREMENTS IN ARGON WITH A LASER HETERODYNE INTERFEROMETER*

by

Ronald N. Cotman**
W. Bruce Johnson

Technical Report No. A-54

November, 1967

*This work was supported by the National Aeronautics and Space Administration, the National Science Foundation, and the Goodyear Aerospace Corporation.

**National Aeronautics and Space Administration Graduate Trainee.

ABSTRACT

The spatially resolved index of refraction of a 4mm bore by 10cm long argon discharge tube has been investigated with a dual wavelength heterodyne interferometer. Measurements were made at pressures of 0.05 Torr, 0.1 Torr, and 0.3 Torr for discharge currents of less than one ampere. The index of refraction changes at the two probe wavelengths (λ=6328Å and λ=11523Å) caused by a change in discharge current have been attributed primarily to the production of plasma electrons and metastable atoms. The contribution from a possible radial gas motion was not observed. Thus, equations were written for the electron and metastable densities in terms of the observed index change at the two probe wavelengths. The values thereby calculated were plotted against current for different radial positions and fill pressures. Finally, the radial distribution of electrons was studied in the 0.1 Torr discharge for a current of 270ma. By the shape of the experimental profile, the dominant electron loss process was confirmed to be ambipolar diffusion rather than free-fall to the walls.

ACKNOWLEDGMENTS

The author wishes to express his appreciation first to Dr. W. B. Johnson for his continuing interest and good counsel. Gratitude is also expressed to Messrs. Edward Parillo and Imre Szilagyi for their excellent glass work, to Mr. Arthur Larsen for his outstanding contribution in developing the apparatus and general analysis technique used, and to Mrs. Martha S. Dybas for typing the manuscript.

The efforts and encouragement of my wife Sharon are also gratefully appreciated.

TABLE OF CONTENTS

ABSTRACT ii

ACKNOWLEDGMENTS iii

LIST OF FIGURES vi

LIST OF TABLES viii

Chapters

I INTRODUCTION
1.1 Purpose of Research 1
1.2 Contents of Report 1

II PRELIMINARY CONSIDERATIONS
2.1 Introduction 3
2.2 Argon Laser Excitation Mechanism 3
2.3 Plasma Measurements with a Laser System 6
2.4 The Index of Refraction of the Argon Discharge. 11

III EXPERIMENTAL APPARATUS
3.1 Introduction 32
3.2 Dual Wavelength Laser Beat-Frequency Interferometer 32
3.3 Frequency Stability. 38
3.4 Window Dispersion 42
3.5 Spatial Resolution 44
3.6 Detection 47
3.7 Summary 49
3.8 Discharge Tubes 50

IV RESULTS OF MEASUREMENTS IN ARGON
4.1 Preliminary Investigations 55
4.2 Separation of Metastable and Electron Densities 64
4.3 Measurements at Other Fill Pressures 71
4.4 Processes Involving Metastable Levels 76
4.5 Electron Distribution 87

Chapters Page

V SUMMARY AND SUGGESTIONS FOR FUTURE WORK 93

APPENDICES

I Miscellaneous Information on AII, NeI, KrI, and XeI 97

II Electronic Circuits 105

LIST OF REFERENCES 111

LIST OF FIGURES

Figure		Page
2.1	Schematic Representation of Argon Laser Processes	4
2.2	Simple Laser Cavity	7
2.3	Rudiments of a Laser Heterodyne System	9
2.4	Partial Energy Level Diagram for AI	18
3.1	Block Diagram for Dual Wavelength Interferometer	34
3.2	Effect of Filter on Detector Input	37
3.3	Dual Wavelength Laser Interferometer	40
3.4	Typical Short Term Stability of Heterodyne Interferometer	41
3.5	Window Dispersion for the Dual Wavelength Cavity	43
3.6	Geometry for Average Spot Size Determination	46
3.7	Argon Discharge Tubes	51
3.8	Electrical Characteristics at Two Pressures for the 10cm Long Argon Discharge Tube	54
4.1	Detector Output Showing Wall Heating Effect	57
4.2	F.M. Detector Outputs Showing Beat Frequency Response at Two Wavelengths	60
4.3	Frequency Shifts vs. Current	62
4.4	Oscillograph of Combined Output vs. Current After Larsen	65
4.5	Electron Density vs. Current	67

Figure		Page
4.6	Total Metastable Density vs. Current	68
4.7	Electron Density vs. Current for Argon at 0.05 Torr	72
4.8	Total Metastable Density vs. Current for Argon at 0.05 Torr	73
4.9	Electron Density vs. Current for Argon at 0.3 Torr	74
4.10	Total Metastable Density vs. Current for Argon at 0.3 Torr	75
4.11	Metastable Density vs. Electron Density for 0.05 Torr.	80
4.12	Metastable Density vs. Electron Density for 0.1 Torr	81
4.13	Metastable Density vs. Electron Density for 0.3 Torr	82
4.14	Radial Profile of Metastable Density at Low Current	83
4.15	Experimental Radial Electron Distribution vs. Pressure	88
4.16	Theoretical and Experimental Values of Electron Density vs. Radius	91
A1.1	Energy-Level Diagram for the Argon-Ion	99
A1.2	Energy-Level Diagram for the Neon Atom	100
A1.3	Energy-Level Diagram for the Krypton Atom	101
A1.4	Energy-Level Diagram for the Xenon Atom	102
A2.1	SCR Inverter Circuit	106
A2.2	Square-Wave Current Pulser	108
A2.3	Turn-Off Circuit	109

LIST OF TABLES

Table		Page
2.1	Predicted Electronic Beat Frequency Shifts at Two Laser Wavelengths	14
2.2	Absorption Oscillator Strengths for Transitions to the $1s_2$ Effective Metastable Level.	21
2.3	Absorption Oscillator Strengths for Transitions to the $1s_4$ Effective Metastable Level.	22
2.4	Absorption Oscillator Strengths for Transitions to the $1s_3$ and $1s_5$ Metastable Levels	23
2.5	Absorption Oscillator Strengths for Resonance Transitions of the Argon Ion	29
2.6	Summary of Refractive Index Changes Evaluated at Two Wavelengths	31
3.1	Average Spot Sizes	45

CHAPTER I

INTRODUCTION

1.1 Purpose of Research

During the past several years, a great deal of interest has been focused on the development of argon-ion lasers. The present research is one outgrowth of this interest. It is now believed that the first step in the excitation mechanism of the argon laser involves electron impact on the atom ground and metastable states. Thus, it is desirable to know the magnitude of the electron and metastable densities as a function of discharge current. The purpose of this experiment, therefore, was to make density measurements in a laser-like argon discharge tube. A dual-wavelength laser heterodyne interferometer was employed. This is a versatile device that senses index of refraction changes in a plasma medium which undergoes density variations. The concept and performance of such a laser interferometer have been described previously,[1,2] but will be reviewed again here.

1.2 Contents of Report

This report has been organized into five chapters. The contents of Chapter I are known. Chapter II begins with a discussion of the proposed argon laser mechanisms. The remaining sections in

Chapter II describe the theory of the laser interferometer and give an analysis for the refractive index of an argon discharge.

The contents of Chapter III describe the specific apparatus. This includes both the laser interferometer and the discharge tubes.

The results of the measurements and a discussion of the results are given in Chapter IV.

Finally, the material in the last chapter summarizes the work done and indicates where future efforts and investigation can be made.

CHAPTER II

PRELIMINARY CONSIDERATIONS

2.1 Introduction

This research was initially undertaken to study a plasma which resembled that of an argon laser. In order to indicate a practical reason for undertaking such a study, we will begin by showing that the electron and metastable atom densities are among the important quantities which appear in the currently proposed laser excitation scheme. Following this discussion, we introduce the concept of using a laser system for measuring a plasma's index of refraction. Then in the last section of this chapter, expressions are obtained for the index of refraction of an argon discharge in terms of the number of electrons, ions, and neutral and metastable atoms which comprise the plasma.

2.2 Argon Laser Excitation Mechanism

The excitation process of the cw or quasi-cw argon laser has been studied quite extensively by E. F. Labuda et al.[3] The results of their work show that the appropriate mechanism involves a three level system such as the one represented in Figure 2.1. The first step of the process is the production of unexcited argon ions by electron impact on both the unexcited neutral atoms and the neutral

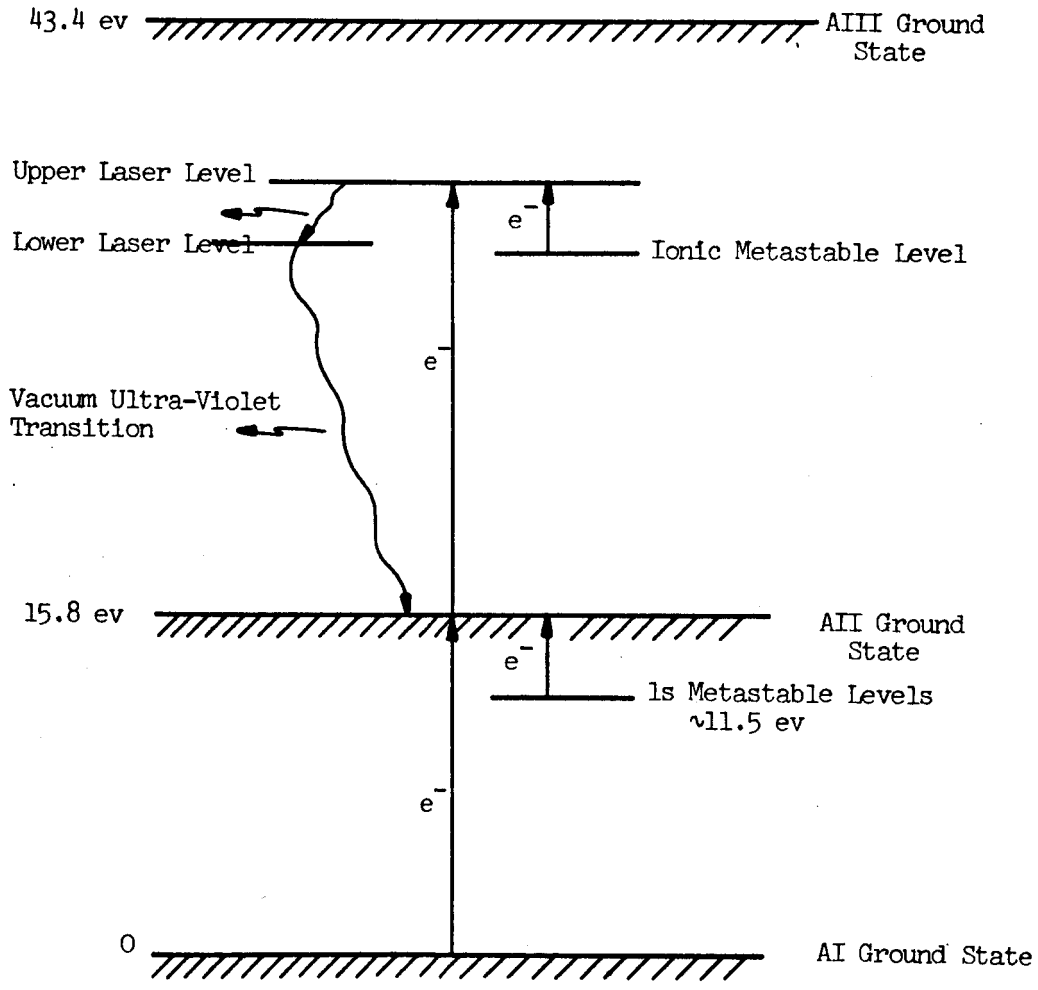

Figure 2.1 Schematic Representation of Argon Laser Processes.

metastable atoms. A meatastable atom is one whose configuration is stable against electric dipole radiation. The lifetime of such an atom is often as long as 10^{-3} seconds so that an appreciable number of these atoms may readily exist in a typical discharge.

In the next step, the upper laser level is populated through electron impact on the unexcited ions and on the various metastable ions. It was once believed that the upper laser level was populated to an appreciable extent by the direct process of electron impact on the atom ground state.[4] Recent measurements indicate, however, that this direct excitation is of relatively minor importance for cw or quasi-cw lasers.[5]

Finally, in order for laser action to occur, it is necessary to satisfy the condition of population inversion. That is, the number of ions in the upper laser level must be greater than the number in some lower level, and of course these levels must be radiatively connected. The principle mechanism for sufficiently depopulating such a lower level is the occurrence of a strong ultra-violet radiative transition to the ion ground state.

From this brief description, therefore, one will recognize the important role of the electrons and various metastable species present in the laser plasma. Thus, with this perspective on the overall laser process we may now consider the fundamental aspects of an experimental method which is ultimately used for measuring electron and metastable densities in a laser-type argon discharge

tube.

2.3 Plasma Measurements With a Laser System

In order to develop the mechanics behind the experimental technique used in these studies, we will begin by considering a simple laser cavity of geometric length L. Such a system is represented in Figure 2.2. We assume that only longitudinal modes will oscillate and initially treat the situation where no plasma tube is present. The condition for resonance is that there be an integral number of half wavelengths between the mirrors. Quantitatively

$$L = q \frac{\lambda}{2} \tag{2.1}$$

where q equals the longitudinal mode number or the number of half wavelengths in L and we assume that the region between mirrors has a unit index of refraction.

If we now put a plasma medium with length ℓ and refractive index n into the laser cavity, L must be interpreted as an optical path length and Equation 2.1 becomes

$$L + (n-1)\ell = q \frac{\lambda}{2} \quad . \tag{2.2}$$

Solving for λ,

$$\lambda = \frac{2[L + (n-1)\ell]}{q} \quad . \tag{2.3}$$

If the index of the plasma is now changed by Δn, the corresponding

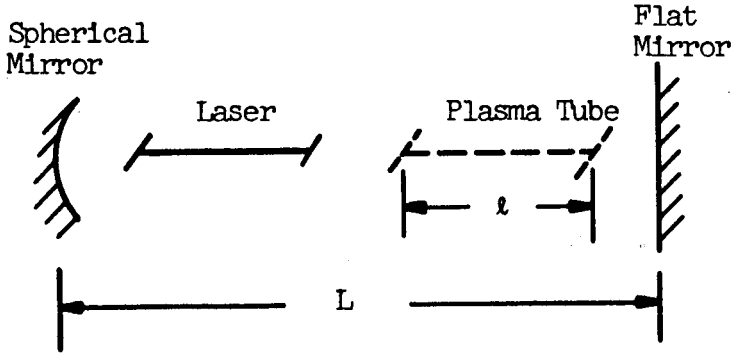

Figure 2.2. Simple Laser Cavity

change $\Delta\lambda$ in wavelength is

$$\Delta\lambda = \frac{2\ell}{q}\Delta n \quad . \tag{2.4}$$

Using the substitutions $\nu = \frac{c}{\lambda}$ and $\Delta\nu = -\frac{c}{\lambda^2}\Delta\lambda$, where c is the free space velocity of light, Equation 2.4 can be solved for the change in the resonant frequency of the cavity with the result

$$\Delta\nu = -\frac{2\ell c}{q\lambda^2}\Delta n \quad . \tag{2.5}$$

If we assume $n \tilde{\nu} 1$ so that $(n-1)\ell << L$, Equation 2.2 gives that $q\lambda \tilde{-} 2L$. Then Equation 2.5 becomes

$$\Delta\nu = -\nu\frac{\ell}{L}\Delta n \quad . \tag{2.6}$$

At this point we consider the possibility of measuring the frequency shift $\Delta\nu$. Since we require enough sensitivity in our method to observe frequency shifts $\sim 10^4 - 10^5$ Hz, no available <u>direct</u> frequency detection for frequencies $\sim 10^{14}$ Hz could measure the necessary one part in 10^{10}. Fortunately, there is an alternative scheme called optical heterodyning. It circumvents the necessity to measure the <u>direct</u> frequency of the single cavity system by combining the outputs of two lasers and measuring the resultant difference or beat frequency. The basic arrangement is given in Figure 2.3. The specification that the spherical mirrors be closely

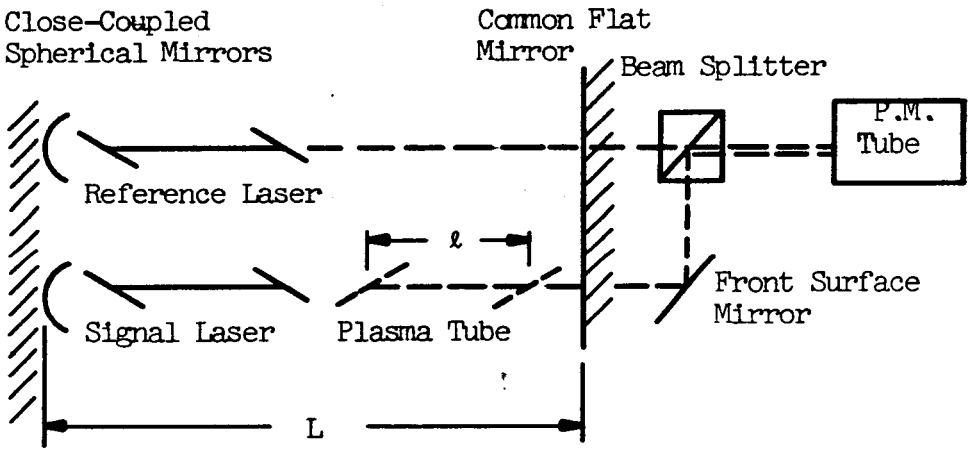

Figure 2.3 Rudiments of a Laser Heterodyne System.

coupled and the flat be common to both lasers is not fundamental to the present argument. However, such an arrangement leads to enhanced frequency stability and will be mentioned again in Chapter III with regard to the actual apparatus used.

We will now give a brief analysis for two lasers operating each in a single longitudinal mode. Assume first that no plasma tube is present. Let the radiation from the reference cavity be a plane wave

$$E_r = A_r \sin\omega_r t \ . \tag{2.7}$$

Similarly, from the signal laser,

$$E_s = A_s \sin(\omega_s t+\phi) \ , \tag{2.8}$$

where ϕ is an arbitrary phase angle.

If these two electric fields are superimposed as indicated in Figure 2.3, the field incident on the photomultiplier tube is

$$E_i = E_s + E_r = A_s \sin(\omega_s t+\phi) + A_r \sin\omega_r t \ . \tag{2.9}$$

Since the current from a photomultiplier tube is proportional to the intensity of the incident radiation and since the photomultiplier tube has a limited frequency response, the photomultiplier output current is

$$i\alpha \left. E_i^2 \right|_{\substack{\text{Within detector} \\ \text{bandwidth}}} = \left(\frac{E_r^2 + E_s^2}{2}\right) + E_r E_s \cos[(\omega_s-\omega_r)t-\phi] \ . \tag{2.10}$$

The first term on the right hand side (R.H.S) of Equation 2.10 is the D.C. component which produces shot noise in the detector. The second term is the A.C. signal component and gives the beat frequency between the lasers. Thus, since $\nu_r \sim \nu_s$, a measure of the beat frequency can be a very sensitive way for determining shifts in the output frequency of one of the lasers.

We now place a plasma tube in the signal laser cavity and consider the effect on the beat frequency of changing the plasma's index. Using Equation 2.6, the beat frequency shift is

$$\Delta(\nu_s - \nu_r) = -\nu_s \frac{\ell}{L} \Delta n \quad . \qquad (2.11)$$

Note that the frequency in Equation 2.6 is the cavity resonance frequency, whereas the beat frequency expressions are in terms of the output frequencies. Indeed these two frequencies are related but in a complicated way.[6] Fortunately, for the conditions of this experiment, these two frequencies can be interchanged with less than 2% error.[7]

Now that a method is available for measuring small frequency shifts, it is necessary to look more carefully into the causes of the change.

2.4 The Index of Refraction of the Argon Discharge

We will assume that an argon discharge consists of electrons, ions, metastable atoms, and neutral atoms. The first three of

these species are formed from the latter under suitable conditions. The manner in which the presence of these various plasma constituents affect the refractive index of the discharge will now be considered in detail.

1. Electronic Dispersion

The change Δn_e in the refractive index due to an electron density change ΔN_e (cm^{-3}) is determined as follows. The dispersion equation for a cold plasma is[8]

$$\kappa(\omega) = 1 - \frac{\omega_p^2}{\omega^2} \quad , \tag{2.12}$$

where $\kappa(\omega)$ is the dielectric constant of the plasma. The quantity ω_p is the electron plasma frequency and is related to the electron density N_e by

$$\omega_p^2 = \frac{4\pi e^2}{m} N_e \quad , \tag{2.13}$$

where e is the electronic charge in electrostatic units and m is the electron's mass in grams. Thus, since the relative permeability μ_r of a plasma is approximately unity, the refractive index due to electrons is

$$n_e(\omega) = \sqrt{\mu_r \kappa(\omega)} \cong \left(1 - \frac{\omega_p^2}{\omega^2}\right)^{1/2} \quad . \tag{2.14}$$

If the R.H.S. of Equation 2.14 is now expanded in a binomial series

assuming $\omega^2 >> \omega_p^2$ we obtain that

$$n_e(\omega) \cong 1 - \frac{\omega_p^2}{2\omega^2} = 1 - \frac{2\pi e^2}{m}\left(\frac{1}{\omega^2}\right)N_e \quad . \tag{2.15}$$

The validity of the above inequality is readily checked. At optical frequencies $\omega^2 \sim 10^{30}(\text{rad/sec})^2$. For a value of $N_e = 10^{13}\text{cm}^{-3}$, $\omega_p^2 = 3.2\text{x}10^{22}(\text{rad/sec})^2$. Thus the assumption $\omega^2 >> \omega_p^2$ is indeed justifiable.

Upon differentiating Equation 2.15, the index change $\Delta n_e(\omega)$ due to a density change ΔN_e is

$$\Delta n_e = -\frac{e^2}{2\pi m}\frac{1}{\nu^2}\Delta N_e \quad . \tag{2.16}$$

From Equation 2.11, the resultant beat frequency shift $\Delta\nu_e$ due to electrons alone is

$$\Delta\nu_e = \frac{e^2}{2\pi m}\frac{\ell}{L}\frac{1}{\nu}\Delta N_e \quad . \tag{2.17}$$

At this point it is perhaps instructive to substitute some numbers into Equation 2.17. Table 2.1 lists the results for a 10 cm long discharge tube in an 86 cm cavity. The frequencies chosen correspond to the well-known helium-neon laser lines at 6328 $\mathring{A}$ and 11523 $\mathring{A}$.

ΔN_e electrons/cm^3	$\lambda_{visible} = 6328\text{Å}$ $\Delta\nu_e(\nu=4.75\times10^{14}\text{Hz})$	$\lambda_{IR} = 11523\text{Å}$ $\Delta\nu_e(\nu=2.6\times10^{14}\text{Hz})$
10^{11}	0.98 kHz	1.8 kHz
10^{12}	9.8	18.0
10^{13}	98.0	180.0

Table 2.1 Predicted Electronic Beat Frequency Shifts at Two Laser Wavelengths

2. Neutral Atom Refractive Index

The index of refraction $n_o(\omega)$ for N_o argon atoms per cm^3 has been measured and satisfies the following relationship[9]

$$n_o(\omega)-1 = \frac{2\pi e^2}{m}\left(\frac{4.25}{671\times10^{30}-\omega^2}\right)N_o \ . \qquad (2.18)$$

For the two laser frequencies used in this experiment, namely $\omega^2 = 8.88\times10^{30}$ and $\omega^2 = 2.68\times10^{30}$ (corresponding to the wavelengths $\lambda = 6328\text{Å}$ and $\lambda = 11523\text{Å}$), Equation 2.18 is approximately independent of frequency with the value

$$n_o-1 = \frac{2\pi e^2}{m}(0.634\times10^{-32})N_o \ . \qquad (2.19)$$

Thus, if the neutral atom density in a particular region of the discharge changes by an amount ΔN_o, either due to consumption in forming electrons, etc. or due to fluctuations caused by local heating, the resultant index change Δn_o is

$$\Delta n_o = \frac{2\pi e^2}{m} (0.634 \times 10^{-32}) \Delta N_o \ . \qquad (2.20)$$

Combining Equation 2.20 with Equation 2.11, then, gives the following beat frequency shift $\Delta \nu_o$:

$$\Delta \nu_o = -\nu \frac{\ell}{L} \frac{2\pi e^2}{m} (0.634 \times 10^{-32}) \Delta N_o \ . \qquad (2.21)$$

3. Atomic Dispersion

The index of refraction $n_i(\omega)$ for N_i atoms per cm^3 in the i^{th} excited state is[10]

$$n_i(\omega) - 1 = \frac{2\pi e^2}{m} N_i \sum_{\substack{k \\ k \neq i}} \frac{f_{ik}}{\omega_{ik}^2 - \omega^2} \ , \qquad (2.22)$$

where f_{ik} is the absorption oscillator strength for the transition from the i^{th} lower state to the k^{th} upper state, and ω_{ik} is the frequency of the radiation emitted in the reverse transition. Equation 2.22 holds as long as ω_i^2 is not "too" close to ω_{ik}^2 . In terms of wavelengths, $|\lambda_{ik} - \lambda| \gtrsim 1\text{Å}$. If a resonance condition exists so that Equation 2.22 no longer holds, an expression which includes collisional damping effects must be

used.[11] Fortunately, the added complication of such considerations is not required in this analysis of argon.

In order to proceed further it is necessary to examine the argon spectrum. With reference to the listings in the M.I.T. Wavelength Tables[12] and C.E. Moore's multiplet table[13] there are no AI or AII (AI and AII refer respectively to neutral and ionized argon) lines within 20Å of either 6328Å or 11523Å. Within 100Å of 6328Å there are 10 AI lines and 3 AII lines, none of which however end on a lower level which is metastable. Within 100Å of 11523Å there are no AII lines. There is one AI transition. It occurs at 11488Å and ends on a level whose resonance radiation is trapped, causing this level to be effectively metastable.

The consequences of the above facts in terms of their relevance to the index of refraction are the following. First, since none of the argon transitions are resonant with the two helium-neon laser lines, index of refraction anomalies are not expected. Secondly, it is noted from Equation 2.22 that the index is directly proportional to the density of atoms in the lower excited state. Thus if this state is metastable, containing a relatively large number of atoms, the resultant index contribution may readily be significant. The extent to which a particular transition involving a metastable or effective metastable level (e.g. the 11488Å line) effects the index depends of course on its oscillator strength and proximity to the probe wavelengths. A

detailed computation is therefore required.

4. Index of Refraction for "Metastable" Atoms

A reasonable starting point for this calculation will be to identify the argon "metastable" states and all transitions which involve these levels. A partial Grotrian or energy level diagram is given in Figure 2.4. The term designations are in Paschen notation. In this system, the small letters s,p,d,f, etc. refer to the orbital angular momentum, ℓ of the jumping electron and correspond to ℓ = 0,1,2,3, etc., respectively. The remaining numbers, however, have no quantum mechanical significance and serve only to label the various levels.[14] Paschen notation was chosen for the present work because of its simplicity and wide usage.

Referring to Figure 2.4, the $1s_3$ and $1s_5$ levels are metastable levels in the true sense since they are stable against electric dipole radiation to the $1p_0$ ground state. The levels $1s_2$ and $1s_4$ both radiate in the ultraviolet to the AI ground state with short natural lifetimes ($\gtrsim 2\times10^{-9}$ seconds) . However, for discharges in which the density of AI ground states is high ($>10^{14}cm^{-3}$) , this resonance radiation is trapped, making the $1s_2$ and $1s_4$ levels effectively metastable.[15] Optical absorption measurements made at Bell Telephone Laboratories indicate that the population densities of all four 1s levels have comparable magnitudes.[16]

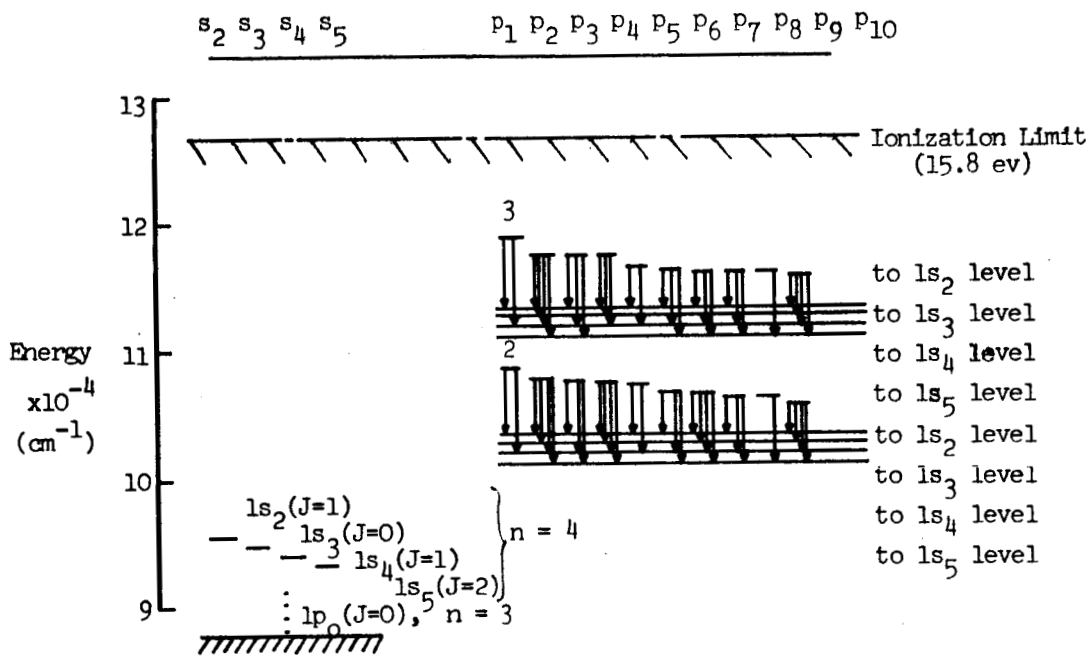

Figure 2.4 Partial Energy Level Diagram for AI. (An example of the above transition notation is as follows. The arrow from the $3p_1$ level to the horizontal line labelled "to ls_2 level" indicates a radiative transition between the $3p_1$ and the ls_2 states).

Before proceeding further, it is desirable to write down the basic format for determining the index of refraction change, Δn_1, due to the formation of a total metastable density, $N_1(cm^{-3})$. (Henceforth the use of the single word metastable will be made without further specifying the "true" or "effective" nature of the 1s levels). In a simple form,

$$\Delta n_1 = (n-1)_{j.e.} + (n-1)_{core} - (n_o-1)_{N_1} \qquad (2.23)$$

The first term on the R.H.S. of Equation (2.23) is the contribution due to the jumping electron alone and thus is calculated by a direct application of Equation 2.22 to the four 1s levels with the sum terms including the appropriate transitions shown in Figure 2.4 . The second term in Equation 2.23 is the index contribution of the excited atom less the part due just to the jumping electron. Finally, the last term on the R.H.S. of Equation 2.23 accounts for the N_1 ground state atoms lost in producing the N_1 excited atoms. Implicit in this statement is the assumption of a simple excitation process which provides metastable atoms directly from ground state atoms. In reality the process may involve many steps. However, these intermediate processes occur very rapidly so that the assumption of losing a ground state atom for each metastable produced should be quite accurate.

The index of refraction due just to the jumping electron will now be determined. Tables 2.2 - 2.4 list the wavelengths,

frequencies, level designations, and oscillator strengths for the transitions indicated in Figure 2.4 . Unfortunately, the National Bureau of Standards has not issued a "best" value listing for the argon oscillator strengths, and the values published by various authors sometimes differ appreciably. In choosing the values listed in the present tables, attention was given to the claimed accuracy and the consistency with which a particular value appeared in the literature. A reference for each value is given in the last column of the tables. Reference 18 is a compilation. The letter "O" in parentheses beside this number designates that this experimental value is due to H.N. Olsen. The oscillator strengths for excitation to the continuum were obtained using the Thomas-Kuhn-Reiche f-sum rule by assuming a single excitation process.[19] This application of the sum rule gives an upper limit for the f value associated with the continuum. It is also noted that the higher lying 3p levels are lumped into the continuum, a reasonable approximation since there is a relatively small energy separation between the 3p levels and the AI ionization limit.

Upon substituting the values from Tables 2.2 - 2.4 into Equation 2.22 we obtain the following long expression for the index of the jumping electron.

Wavelength λ_{ik}(Å)	Frequency ω_{ik}(rad/sec)	k^{th} Upper Level Designation	i^{th} Lower Level Designation	Oscillator Strength f_{ik}	Reference Number
11488.11	1.644×10^{15}	$2p_{10}$	$1s_2$	0.00356	17
9784.50	1.93×10^{15}	$2p_8$	"	0.0256	17
9354.22	2.02×10^{15}	$2p_7$	"	0.00842	17
9224.50	2.05×10^{15}	$2p_6$	"	0.125	17
8578.05	2.20×10^{15}	$2p_5$	"	Negligible	17
8521.44	2.22×10^{15}	$2p_4$	"	0.115	18(O)
8408.21	2.24×10^{15}	$2p_3$	"	0.274	18(O)
8264.52	2.28×10^{15}	$2p_2$	"	0.134	18(O)
7503.87	2.51×10^{15}	$2p_1$	"	0.122	18(O)
4702.32		$3p_{10}$	"		
4628.44		$3p_8$	"		
4596.10	Include	$3p_7$	"		
4589.28	these in	$3p_6$	"		
4510.73	continuum	$3p_5$	"		
4345.17		$3p_4$	"		
4333.56		$3p_3$	"		
4335.34		$3p_2$	"		
4259.36		$3p_1$	"		
Continuum	$\gtrsim 6.0 \times 10^{15}$			0.192[a]	

[a]Obtained using the f-sum rule with $\Sigma f = 1$.

Table 2.2 Absorption Oscillator Strengths for Transitions to the $1s_2$ Effective Metastable Level.

Wavelength λ_{ik}(Å)	Frequency ω_{ik}(rad/sec)	k^{th} Upper Level Designation	i^{th} Lower Level Designation	Oscillator Strength f_{ik}	Reference Number
9657.78	1.95×10^{15}	$2p_{10}$	$1s_4$	0.0658	17
8424.65	2.24×10^{15}	$2p_8$	"	0.247	18(O)
8103.69	2.32×10^{15}	$2p_7$	"	0.191	18(O)
8006.16	2.36×10^{15}	$2p_6$	"	0.0816	18(O)
7514.65	2.51×10^{15}	$2p_5$	"	0.108	18(O)
7471.65	2.53×10^{15}	$2p_4$	"	0.00301	17
7383.98	2.56×10^{15}	$2p_3$	"	0.118	18(O)
7272.94	2.59×10^{15}	$2p_2$	"	0.128	18(O)
6677.30	2.83×10^{15}	$2p_1$	"	Negligible	17
4363.79		$3p_{10}$	"		
4300.10	Include these in Continuum	$3p_8$	"		
4272.17		$3p_7$	"		
4266.29		$3p_6$	"		
4198.32		$3p_5$	"		
4054.52		$3p_4$	"		
4044.42		$3p_3$	"		
4045.96		$3p_2$	"		
3979.71		$3p_1$	"		
Continuum	$\gtrsim 6.3\times10^{15}$			0.057[a]	

[a]Obtained using the f-sum rule with $\Sigma f = 1$.

Table 2.3 Absorption Oscillator Strengths for Transitions to the $1s_4$ Effective Metastable Level.

Wavelength λ_{ik}(Å)	Frequency ω_{ik}(rad/sec)	k^{th} Upper Level Designation	i^{th} Lower Level Designation	Oscillator Strength f_{ik}	Reference Number
10470.05	1.80×10^{15}	$2p_{10}$	$1s_3$	0.0435	17
8667.94	2.18×10^{15}	$2p_7$	"	0.108	17
7948.18	2.37×10^{15}	$2p_4$	"	0.417	18(0)
7724.21	2.44×10^{15}	$2p_2$	"	0.327	17
4522.32	Include these in continuum	$3p_{10}$	"		
4191.03		$3p_4$	"		
4181.88		$3p_2$	"		
Continuum	26.14×10^{15}		"	0.105[a]	
9122.97	2.07	$2p_{10}$	$1s_5$	0.130	17
8115.31	2.32	$2p_9$	"	0.214	18(0)
8014.79	2.36	$2p_8$	"	0.0720	18(0)
7723.76	2.46	$2p_7$	"	0.0295	17
7635.11	2.48	$2p_6$	"	0.178	18(0)
7147.04	2.64	$2p_4$	"	0.00597	17
7067.22	2.67	$2p_3$	"	0.0428	17
6965.43	2.71	$2p_2$	"	0.0233	18(0)
4251.19	Include these in continuum	$3p_{10}$	"		
4200.68		$3p_9$	"		
4190.71		$3p_8$	"		
4164.18		$3p_7$	"		
4158.59		$3p_6$	"		
3947.50		$3p_3$	"		
3948.98		$3p_2$	"		
Continuum			"	0.304[a]	

[a]Obtained using the f-sum rule with $\Sigma f = 1$.

Table 2.4 Absorption Oscillator Strengths for Transition to the $1s_3$ and $1s_5$ Metastable Levels.

$$(n(\omega)-1)_{j.e.} = \frac{2\pi e^2}{m}\{N_{ls_2}[\frac{0.00356}{(1.644\times10^{15})^2-\omega^2} + \frac{0.0256}{(1.93\times10^{15})^2-\omega^2} +\cdot$$

$$\cdot+ \frac{0.0084}{(2.02\times10^{15})^2-\omega^2} + \frac{0.125}{(2.05\times10^{15})^2-\omega^2} + \frac{0.115}{(2.22\times10^{15})^2-\omega^2} +\cdot$$

$$\cdot+ \frac{0.274}{(2.24\times10^{15})^2-\omega^2} + \frac{0.134}{(2.28\times10^{15})^2-\omega^2} + \frac{0.122}{(2.51\times10^{15})^2-\omega^2} +\cdot$$

$$\cdot+ \frac{0.192}{(6.0\times10^{15})^2-\omega^2}]+ N_{ls_3}[\frac{0.0435}{(1.8\times10^{15})^2-\omega^2} +\cdot$$

$$\cdot+ \frac{0.108}{(2.18\times10^{15})^2-\omega^2} + \frac{0.417}{(2.37\times10^{15})^2-\omega^2} + \frac{0.327}{(2.44\times10^{15})^2-\omega^2} +\cdot$$

$$\cdot+ \frac{0.105}{(6.14\times10^{15})^2-\omega^2}]+N_{ls_4}[\frac{0.066}{(1.95\times10^{15})^2-\omega^2} +\cdot$$

$$\cdot+ \frac{0.247}{(2.24\times10^{15})^2-\omega^2} + \frac{0.191}{(2.32\times10^{15})^2-\omega^2} + \frac{0.0816}{(2.36\times10^{15})^2-\omega^2} +\cdot$$

$$\cdot+ \frac{0.108}{(2.51\times10^{15})^2-\omega^2} + \frac{0.00301}{(2.53\times10^{15})^2-\omega^2} + \frac{0.118}{(2.56\times10^{15})^2-\omega^2} +\cdot$$

$$\cdot+ \frac{0.128}{(2.59\times10^{15})^2-\omega^2} + \frac{0.057}{(6.3\times10^{15})^2-\omega^2}] +\cdot$$

$$\cdot+ N_{ls_5}[\frac{0.130}{(2.07\times10^{15})^2-\omega^2} + \frac{0.214}{(2.32\times10^{15})^2-\omega^2} +\cdot$$

$$\cdot+\frac{0.072}{(2.36\times10^{15})^2-\omega^2}+\frac{0.0295}{(2.46\times10^{15})^2-\omega^2}+\frac{0.178}{(2.48\times10^{15})^2-\omega^2}+\cdot$$

$$\cdot+\frac{0.00597}{(2.64\times10^{15})^2-\omega^2}+\frac{0.0428}{(2.67\times10^{15})^2-\omega^2}+\frac{0.0233}{(2.71\times10^{15})^2-\omega^2}+\cdot$$

$$\cdot+\frac{0.304}{(6.3\times10^{15})^2-\omega^2}\,]\}\qquad(2.24)$$

The quantities N_{1s_2}, N_{1s_3}, N_{1s_4}, and N_{1s_5} refer to the population densities of the $1s_2$, $1s_3$, $1s_4$ and $1s_5$ levels, respectively. If Equation 2.24 is next evaluated at the angular frequencies $\omega = 2.98\times10^{15}$ and $\omega = 1.64\times10^{15}$ which correspond to the 6328Å visible and 11523Å infrared (IR) laser lines, resepctively, the following equations result.

$$(n(\omega=2.98\times10^{15})-1)_{j.e.} = -\frac{2\pi e^2}{m}\times10^{-32}(21.1N_{1s_2}+27.0N_{1s_3}+\cdot$$
$$\cdot+31.1N_{1s_4}+23.0N_{1s_5})\qquad(2.25a)$$

$$(n(\omega=1.64\times10^{15})-1)_{j.e.} = +\frac{2\pi e^2}{m}\times10^{-3}(59.6N_{1s_2}+37.7N_{1s_3}+\cdot$$
$$\cdot+30.3N_{1s_4}+27.0N_{1s_5})\,.\qquad(2.25b)$$

In order to further simplify Equations 2.25, we will assume that

the four 1s levels are in thermal equilibrium. Such an approximation is appropriate for these levels since the energy separating them ($\lesssim 800\ cm^{-1}$) is less than or equal to the thermal energy of the gas atoms. Hence, a high degree of collisional mixing from atom-atom, near resonance collisions occurs at elevated gas temperatures.[20]

Therefore, let the <u>total</u> density of 1s levels be N_1. The fractional contribution of the four separate levels to this total number is then obtained from the Maxwellian or equilibrium distribution law which states[21] that the population density N_i of the i^{th} excited state is

$$N_i = Fg_i e^{E_i/kT} \tag{2.26}$$

where F is a function of the total atom density and gas temperature, g_i is the statistical weight of the i^{th} level, E_i is the energy of the i^{th} level, k is Boltzmann's constant, and T is the gas temperature. Since the four levels have approximately the same energy, the contribution from the exponential factor in Equation 2.26 is nearly constant and the desired ratios will be obtained directly from the relative magnitudes of the statistical weights. In terms of the total angular momentum quantum number J, the statistical weight is

$$g_i = 2J+1 \tag{2.27}$$

The J values for the 1s levels are given in Figure 2.4 . Therefore, upon substituting in Equation 2.27 and forming ratios, the 1s level population densities as a function of the total 1s density become

$$N_{1s_2} = 0.250\ N_1$$

$$N_{1s_3} = 0.083\ N_1$$

$$N_{1s_4} = 0.250\ N_1$$

$$N_{1s_5} = 0.417\ N_1 \qquad (2.28)$$

Direct substitution of Equations 2.28 into Equations 2.25 gives the following final expressions for the jumping electron index.

$$(n(\omega = 2.98\text{x}10^{15})-1)_{j.e.} = \frac{2\pi e^2}{m}\text{x}10^{-32}(-24.9\ N_1) \qquad (2.29a)$$

$$(n(\omega = 1.64\text{x}10^{15})-1)_{j.e.} = \frac{2\pi e^2}{m}\text{x}10^{-32}(+35.8\ N_1). \qquad (2.29b)$$

It is next necessary to compute the index of refraction of the metastable cores. In this useage, a core is the part of the atom which includes the outer electrons less the single jumping electron. Referring to Figure 2.4 again, it is noted that the principal quantum number n for the ground state is 3 whereas it equals 4 for the 1s levels. Because of this fact, the shielding effect of the jumping electron will be neglected and the

core treated as an argon ion. The index of refraction for an ion must therefore be determined. Table 2.5 lists the wavelengths, angular frequencies, level designations, and oscillator strengths for argon ion resonance transitions. A resonance transition is one in which an electron jumps from the ground state to some excited level. The nomenclature which is used for the level assignments is the Russell-Saunders or L-S coupling notation and is explained in Appendix I. Resonance states lying above the 3d levels are included in the continuum. The values for the oscillator strengths are based on the Coulomb approximation and were obtained from Griem.[22]

When the values from Table 2.5 are substitued into Equation 2.22, we obtain the following expression for the ion index n_I

$$n_I(\omega)-1 = \frac{2\pi e^2}{m} N_I\left[\frac{0.0485}{(2.62\times10^{16})^2-\omega^2} + \frac{0.0248}{(2.81\times10^{16})^2-\omega^2} + \cdots\right.$$

$$\left. + \frac{0.872}{(2.84\times10^{16})^2-\omega^2} + \frac{0.055}{(4.20\times10^{16})^2-\omega^2}\right] . \qquad (2.30)$$

The quantity N_I is the ion number density. For the two frequencies used in this experiment, Equation 2.30 is almost constant and has the value

$$n_I-1 = \frac{2\pi e^2}{m} \times 10^{-32}(0.123\ N_I) . \qquad (2.31)$$

We have now completed a calculation of the first two terms on

Wavelength[23] (Å)	Frequency (rad/sec)	Upper Level Designation	Lower Level Designation	Oscillator Strength
723.4	~2.62x10^{16}	4s $^2P_{3/2}$	3p^5 $^2P^o_{3/2}$	0.0410
718.1		4s $^2P_{1/2}$	"	0.00747
672.8	~2.81x10^{16}	4s' $^2D_{3/2}$	"	0.00252
671.9		4s' $^2D_{5/2}$	"	0.0223
664.6	~2.84x10^{16}	3d $^2D_{3/2}$	"	0.0862
661.9		3d $^2D_{5/2}$	"	0.786
Continuum	$\gtrsim$4.20x10^{16}		"	0.055[a]

[a]Calculated from the f-sum rule with $\Sigma f = 1$.

Table 2.5 Absorption Oscillator Strengths for Resonance Transitions of the Argon Ion.

the R.H.S. of Equation 2.23 for the index of refraction change due to metastables. The third term is also known, though, since it can be obtained directly from Equation 2.19. Therefore a straightforward substitution of Equations 2.29a, 2.29b, 2.31 (with N_I replaced by N_1), and 2.19 (with N_o replaced by N_1) into Equation 2.23 gives that the metastable index of refraction changes at the two probe wavelengths are

$$\Delta n_1(\lambda=6328\mathring{A}) = \frac{2\pi e^2}{m} x10^{-32}(-25.4\ N_1) \ , \qquad (2.32a)$$

and

$$\Delta n_1(\lambda=11523\mathring{A}) = \frac{2\pi e^2}{m} x10^{-32}(36.3\ N_1) \ . \qquad (2.32b)$$

5. Index of Refraction for Ionization

The ionization process in a discharge involves the production of electrons and ions at the expense of argon atoms. The change in the index of refraction of a gas due to ionization can therefore be expressed as

$$\Delta n_{ionization} = (n_e-1)+(n_I-1)-(n_o-1) \ . \qquad (2.33)$$

The first two terms on the R.H.S. are for the electrons and ions produced while the last term accounts for the atoms lost. In a typical discharge the density of ions is approximately equal to the electron density. Thus, Equation 2.33 is readily evaluated in terms of the electron density N_e. Upon substituting Equations 2.15, 2.31 (with N_I replaced by N_e), and 2.19 (with N_o replaced by N_e) into Equation 2.33 we obtain the following results.

$$\Delta n_{ionization}(\lambda=6328\mathring{A}) = \frac{2\pi e^2}{m} x10^{-32}(-11.8\ N_e) \qquad (2.34a)$$

$$\Delta n_{ionization}(\lambda=11523\mathring{A}) = \frac{2\pi e^2}{m} x10^{-32}(-37.7\ N_e)\ . \qquad (2.34b)$$

6. Summary

For comparison purposes, the above results for index of refraction changes in an argon discharge are summarized in Table 2.6 .

It is recalled that Δn_1 refers to the metastable index shift and was given by Equations 2.32a and 2.32b. The entries in the third column headed $\Delta n_{ionization}$ were obtained from Equations 2.34. Column four lists the index change due just to the production of electrons. By comparing this column with column three we see that there is only a small error introduced at optical frequencies if the effects of ions produced and neutrals consumed in the ionization process are ignored. Finally, the last column refers to the index change caused by a shift of argon atoms and was rewritten from Equation 2.20.

Probe Wavelength	Δn_1	$\Delta n_{ionization}$	Δn_e	Δn_o
$6328\mathring{A}$	$\frac{2\pi e^2}{m} x10^{-32}\{-25.4N_1$	$-11.8N_e$	$-11.3N_e$	$+0.634\Delta N_o$
$11523\mathring{A}$	$\{+36.3N_1$	$-37.7N_e$	$-37.1N_e$	$+0.634\Delta N_o$

Table 2.6 Summary of Refractive Index Changes Evaluated at Two Wavelengths.

CHAPTER III

EXPERIMENTAL APPARATUS

3.1 Introduction

In Chapter II, the concept of a laser interferometer was introduced and expressions were obtained for the index of refraction of an argon discharge. The results of the index of refraction calculations showed that important index changes are due to electrons, metastable atoms, and possibly local shifts in atom density. Thus, in order to satisfactorily study an argon discharge with a laser system , it will be necessary to probe the plasma with radiation of different wavelengths. Consequently, the purpose of the first sections of this chapter is to describe the particular dual wavelength laser system which was used in this experiment. This description is intended to be reasonably brief. The emphasis rests only on those facts which are particularly pertinent to the present work. A much more complete analysis has been carried out by A. B. Larsen.[24]

In the last section of this chapter, we describe the physical and electrical characteristics of the experimental discharge tubes.

3.2 Dual Wavelength Laser Beat-Frequency Interferometer

A detailed schematic representation for the laser system

particular to this experiment is given in Figure 3.1. The two helium-neon lasers operate on the 6328Å and 11523Å neon transitions simultaneously. The beams emerging from the common flat mirror are superimposed by means of a mirror and a beam splitter. The alignment tolerance on this superposition is that the angular separation between the beams be less than 2 minutes of arc. These superimposed beams then pass through optical filters and are detected with photomultipliers. The 6328Å filter removes all radiation except the desired visible laser light. Similarly, the 11523Å filter allows only the infrared laser beam to pass.

Following the photomultipliers on both channels are identical F.M. detectors. An F.M. detector is a device which produces a voltage output proportional to the frequency of the "sinusoidal" signal fed into it. In this application therefore, the F.M. detector outputs give a measure of the difference or beat frequency between the lasers.

The wide-band F.M. detector unit (two of which are used) was designed especially for this apparatus by A. B. Larsen. The output is a linear function of the input frequency and is about -2.5 volts per mHz over the usable range of 0-2 MHz. Further, the detector output is independent of the input level for signals which exceed 50 mv peak to peak. The effect of noise on the input signal was minimized by using an arrangement of Schmidt triggers and flip-flops to "count" the number of times the signal alternately crosses

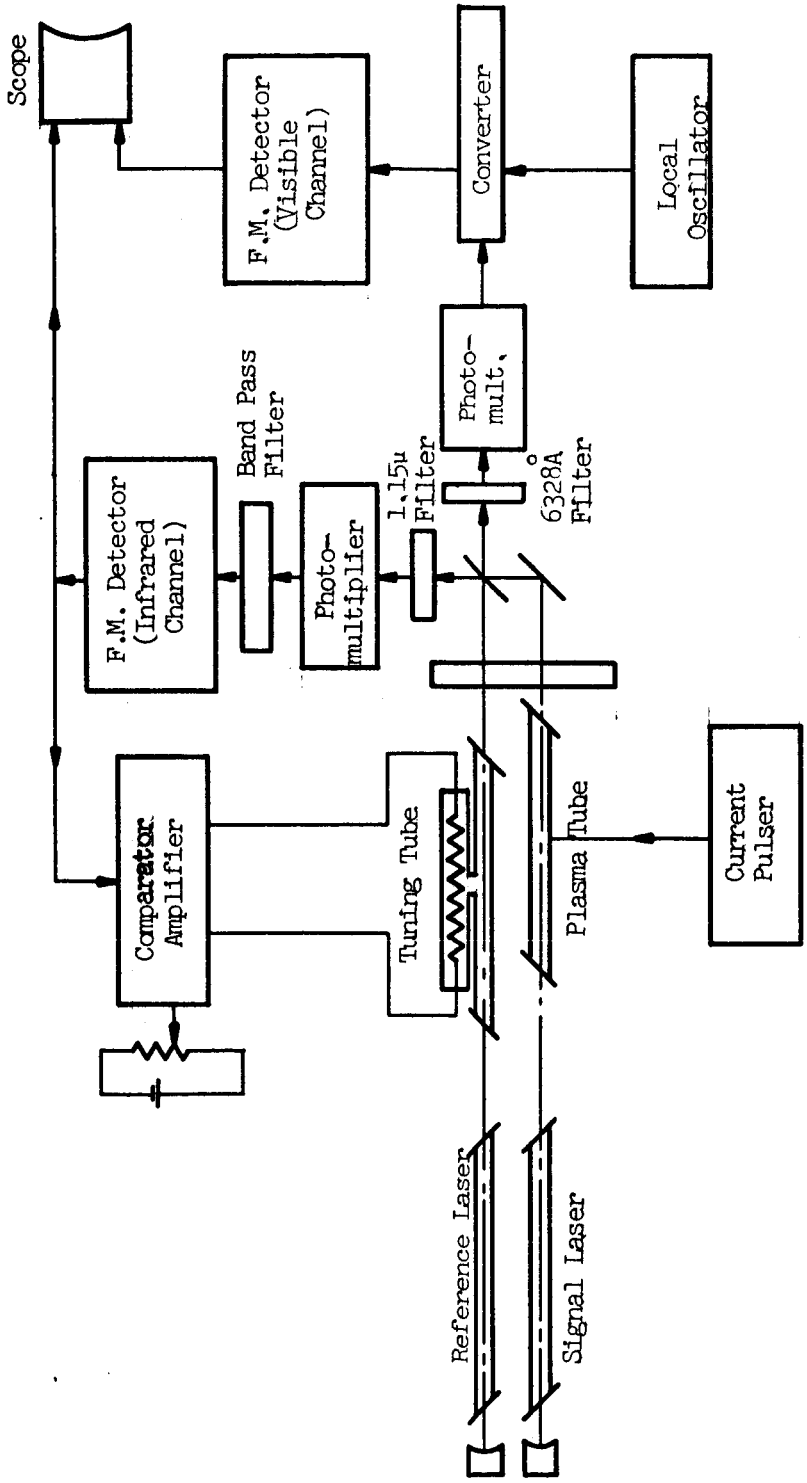

Figure 3.1 Block Diagram for Dual Wavelength Interferometer.

two reference voltage levels. RC filters are then used to smooth the pulses from the flip-flops and thus allow real-time observation of the detector output. For all of the measurements made in this experiment, a detector time constant of 5 microseconds was used on both detectors.

The tuning tube, which is also shown in Figure 3.1, is used for adjusting the value of the beat frequency. It consists of two chambers which are connected at the middle and are filled with air. One of the chambers is fitted with Brewster angle windows and is situated in the reference laser cavity. The other chamber contains a tungsten wire whose temperature is readily varied by changing the current which passes through it. Thus, if the current is increased, the temperature of the wire and hence the pressure of the air in this chamber is increased. This then produces a net flow of gas atoms into the adjoining chamber, leading to an increased refractive index. By Equation 2.6, this increase in refractive index produces a decrease in the output frequency of the reference laser and therefore changes the beat frequency. In practice, the tuning tube is used in conjunction with a feedback circuit to maintain a 1 MHz beat frequency on the infrared channel. The error signal is obtained by comparing the voltage output from this channel's F.M. detector with a reference voltage. The electronics of this comparator are such that stable closed-loop operation is possible only when the signal laser output frequency is <u>greater</u> than the reference laser. Thus it is possible to tell whether a

particular current pulse through the discharge tube produces a positive or a negative change in beat frequency. The time response of the feedback circuit is made slow relative to the current pulse duration but fast enough to stabilize the beat frequency against the effects of thermal fluctuations and low frequency accoustical vibrations. Typically, the feedback responds to fluctuations with frequencies less than 50 Hz.

When the beat frequency on the infrared channel is tuned to 1 MHz by the feedback circuit, the visible channel beat frequency is also stabilized but at some value which is anywhere between 0 and 87 MHz. However, the F.M. detectors are usable only over the range 0-2 MHz. Therefore, a converter or mixer circuit is employed to bring the visible signal into this frequency range.

The final item in Figure 3.1 which should be pointed out is the 1 mHz band pass filter located between the phototube and F.M. detector on the infrared channel. This filter has a band-width of several hundred kHz and is required because of the excessive noise which accompanies the infrared beat frequency signal. For example, the unfiltered and the filtered beat frequency signals are shown in Figure 3.2. If the filter is removed from the circuitry or if its band width is increased beyond some 400 kHz, the F.M. detector is unable to properly demodulate the infrared signal for undistorted oscillographic observation. The required presence of this filter, therefore, sets a limit on the band-width of the infrared channel

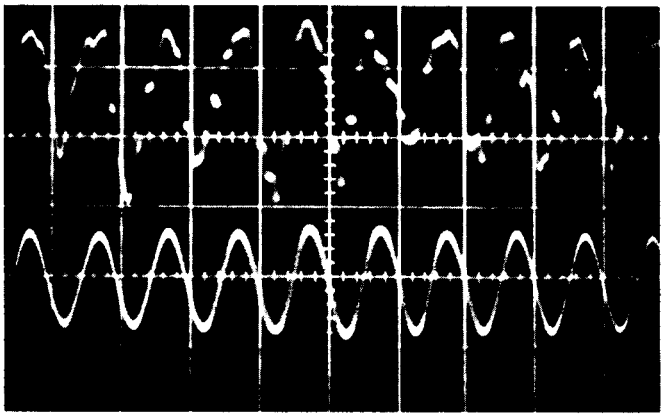

Upper Trace:
Unfiltered Input
at 1.0 volt/cm.

Lower Trace:
Filtered Input
at 1.0 volt/cm.

Horizontal Sweep:
1μsec/cm.

Figure 3.2 Effect of Filter on
Detector Input.

or on the entire system if measurements must be made at both wavelengths. To date, the largest beat frequency shift successfully recorded was 350 kHz. Typically, however, one is restricted to observe shifts which are less than 250 kHz.

In the next several sections, various additional aspects of the apparatus are discussed in order to give the reader a better indication of the system's capabilities.

3.3 Frequency Stability

Referring to Equation 2.3 it is apparent that any disturbance which changes the cavity length, L , or the index of refraction of the air within the cavity will produce a change in the cavity resonance wavelength and hence the beat frequency. There are many such disturbances, any of which in an ordinary environment could easily cause frequency instabilities of several megahertz. They include temperature fluctuations, accoustical vibrations, and air currents. When the present apparatus was set up, special precautions were taken to produce an extraordinary environment and thereby minimize these effects. For example, in order to "isolate" the system from building vibrations, the apparatus was assembled on the Wickenden Building's ground floor atop a cast iron machinist's layout table weighing approximately one ton. This table was itself supported by a thick column of plywood, packing material and another machine shop table, all of which was floated on a cushion of air provided by several automobile inner tubes. Furthermore,

the laser cavities were arranged in the close-coupled configuration alluded to earlier in Chapter II.

The effect of air currents through the cavity was appreciably reduced by the use of drift tubes. Drift tubes are sleeves which enclosed the regions intermediate between the mirrors, lasers, tuning tube, and discharge tube. Also the entire interferometer was covered with a plastic box.

A photograph of the apparatus showing the iron table, the drift tubes, and part of the plywood pedestal is given in Figure 3.3. The plastic box was removed for photographic clarity. A 10 cm long argon discharge tube held by a micrometer slide arrangement is also shown quite clearly in this picture.

In spite of the above precautions the free-running system (i.e. with no feedback) had an optimum stability of about $\pm$500 kHz over a period of a few minutes. Increased stability was obtained however by using the feedback system described in Section 3.1. For closed loop operation, typical long term ($\sim$minutes)stabilities were $\pm$50kHz.

For the measurements made in this experiment, beat frequency shifts corresponding to current pulses of about 500 microseconds duration were observed. A typical example of the associated short term stability is given in Figure 3.4. The F.M. detector outputs for both the visible and infrared channels are shown.

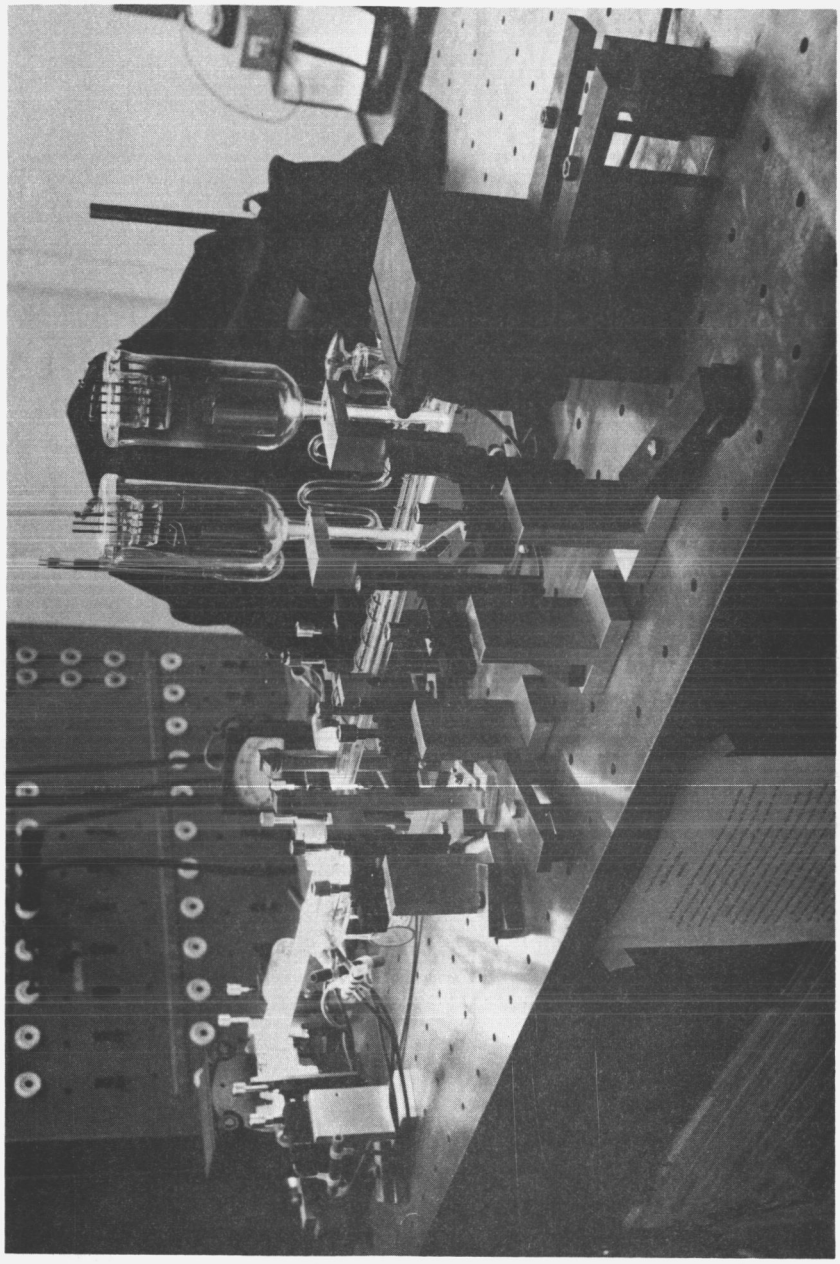

Figure 3.3 Dual Wavelength Laser Interferometer.

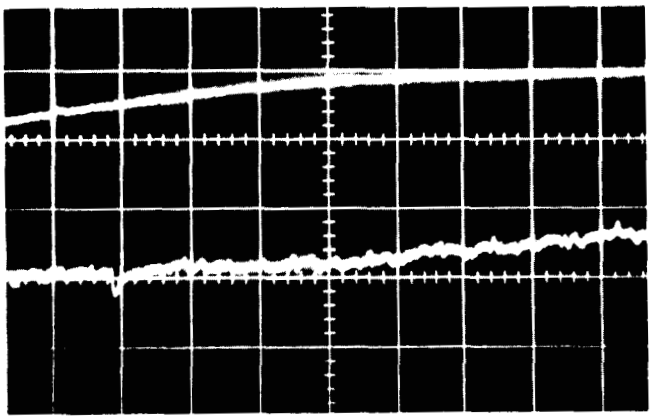

Upper trace:
Visible Channel F.M.
Detector Output at
40kHz/cm.

Lower Trace:
IR Channel F.M.
Detector Output at
40kHz/cm.

Horizontal Sweep:
200μsec/cm.

Figure 3.4 Typical Short Term Stability of Heterodyne Interferometer.

3.4 Window Dispersion

Since the index of refraction of glass is a function of frequency, the infrared and visible laser beams are refracted by different amounts as they pass through the Brewster angle windows of the laser cavities. Indeed the positions of the beams in the cavity depend on the number, thickness, and relative orientations of these windows. Furthermore there are three requirements on the beam positions. They are the following ones.

1. The two beams must coincide within the plasma tube so that the same volume is probed by both beams.

2. The cavity should be optimally aligned for both wavelengths simultaneously.

3. The infrared and visible beams should be parallel and separated by the same distance at the flat mirror. This requirement is necessary for simultaneous heterodyning on both wavelengths.

There are a great variety of cavity configurations which satisfy these conditions. The arrangement utilized in the present work has a trapezoidal geometry and is shown schematically in Figure 3.5 . Relative beam positions are also given. Qualitatively, the index of glass at visible wavelengths is greater than at infrared wavelengths. Hence by Snell's law, the visible beam is bent more strongly as it enters a window.

Referring to Figure 3.5, the beams at both wavelengths are coincident at the spherical mirrors. This requirement is imposed by

Visible Beam

Infrared Beam

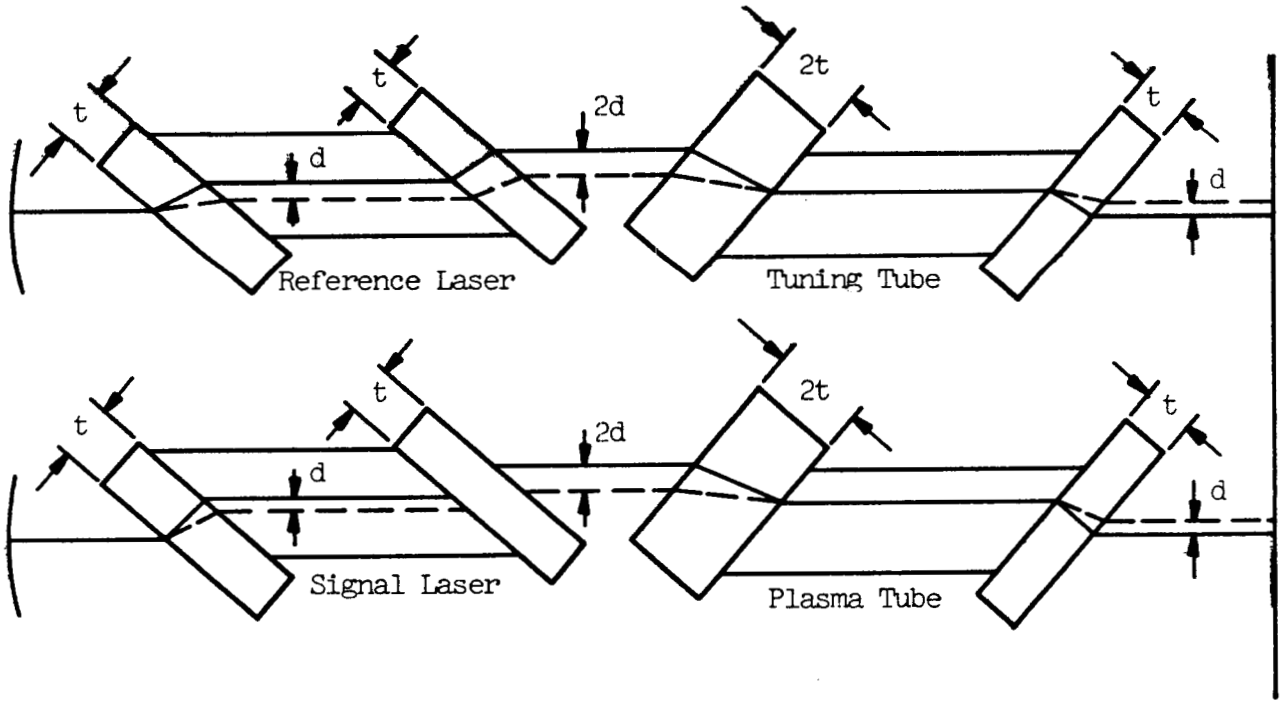

Figure 3.5 Window Dispersion for the Dual Wavelength Cavity.

condition 2 above and insures optimum simultaneous alignment for a plane-spherical cavity. The infrared and visible beams are then refracted by the first window of thickness t. Their separation in both lasers is some distance d. As the beams enter the following thickness t of glass they are refracted again, emerging with a separation of $2d$. When the beams next enter the windows having a thickness $2t$, they are bent in a direction which brings the beams together again. In the plasma tube, therefore, the beams are coincident and condition 1 above is satisfied. Finally, the beams are once more refracted as they pass through the last window of thickness t, and impinge on the flat mirror separated by the distance d. Because of symmetry, this same separation d exists between the infrared and visible beams emerging from the last window on the plasma tube as well as from the last window on the tuning tube. Hence condition 3 is also met.

3.5 Spatial Resolution

The spatial resolution of this interferometer is determined by the spot size of the laser beams. Following the definition of Boyd and Gordon,[25] the spot size is the distance from the axis of the beam to the point where the field of the TEM_{ooq} mode falls to $\frac{1}{e}$ of its axial value. The spot size w_f on the flat mirror and the spot size w_s on the spherical mirror of radius R_M are given by the formulas[26]

$$w_f = \left(\frac{\lambda L}{\pi}\right)^{1/2} \left[\frac{(R_M - L)}{L}\right]^{1/4}, \qquad (3.1)$$

and

$$w_s = \left(\frac{\lambda L}{\pi}\right)^{1/2} \left[\frac{R_M^2}{L(R_M - L)}\right]^{1/4} . \qquad (3.2)$$

Referring to Figure 3.6, an expression derived from ray optics for the average spot size w_a within the plasma tube, is

$$w_a = w_f + \left(\frac{h + \frac{\ell}{2}}{L}\right)(w_s - w_f) , \qquad (3.3)$$

where h is the distance from the flat mirror to the discharge tube. The word "average" in this usage means the value at the middle of the discharge tube which is at a distance $h + \frac{\ell}{2}$ from the flat mirror. For the values used in this experiment (L = 86 cm, R_M = 100 cm, h = 5 cm, ℓ = 10 cm) the average spot sizes at the two laser wavelengths are listed in Table 3.1 .

The spot size of the visible beam was measured at a point 10 cm from the flat mirror. The observed value was in good agreement with the one given in Table 3.1 .

Wavelength (Å)	w_a (mm)
6328	0.32
11523	0.42

Table 3.1 Average Spot Sizes.

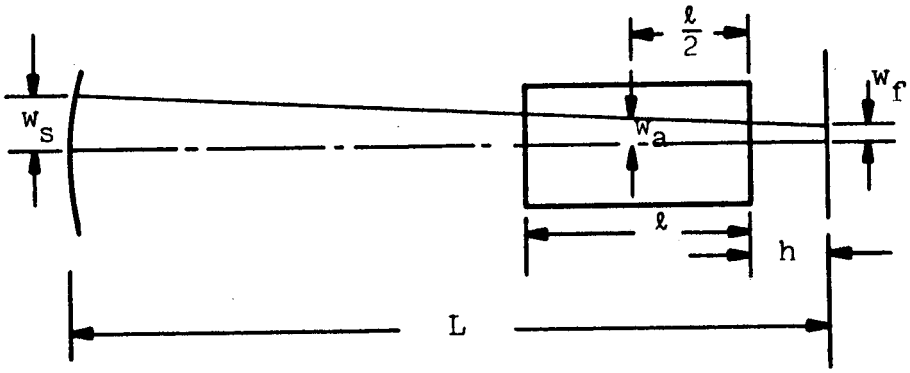

Figure 3.6 Geometry for Average Spot Size Determination.

3.6 Detection

The photomultiplier tube detectors are at the very heart of the heterodyne process. Recalling Equation 2.10, the phototube output current is

$$i = \frac{\gamma}{2}\{(E_r^2 + E_s^2) + 2E_rE_s\cos[(\omega_s-\omega_r)t-\phi]\} \quad , \tag{3.4}$$

where γ is the proportionality constant between current and field intensity. This constant is further given by the expression[27]

$$\gamma = \left(\frac{\varepsilon_o}{\mu_o}\right)^{1/2} \frac{Ae\eta}{2h\nu} \quad , \tag{3.5}$$

where A is the area of the photosurface and η is the quantum efficiency of the photocathode at either ω_r or ω_s (since they are nearly equal).

The D.C. current component in Equation 3.4 is

$$\bar{i} = \frac{\gamma}{2}(E_r^2 + E_s^2) \quad , \tag{3.6}$$

and generates noise in the detector. This so-called shot noise has, associated with it, an r.m.s. current given by[28]

$$\bar{i}_n^2 = 2eB\bar{i} = eB\gamma(E_r^2 + E_s^2) \quad , \tag{3.7}$$

where B is the bandwidth of the system.

The A.C. current in Equation 3.4 is, of course, the signal

component. Its r.m.s. value is

$$\overline{i_s^2} = (\gamma E_r E_s)^2 \tag{3.8}$$

Thus, if shot noise is the primary source of noise in the phototubes, the signal to noise ratio $(\frac{S}{N})$ for the system is

$$\frac{S}{N} = \frac{\overline{i_s^2}}{\overline{i_n^2}} = \frac{\gamma}{eB} \left(\frac{E_r^2 E_s^2}{E_r^2 + E_s^2}\right) . \tag{3.9}$$

This assumption regarding the importance of shot noise has been checked by blocking the beams falling onto the photomultiplier tubes and noting that the current goes to zero.

With regard to the present experimental apparatus, the signal-to-noise performance on the infrared channel is of particular interest. At best, the signal to noise ratio for this wavelength is poor. This fact is due primarily to the low quantum efficiencies at these frequencies. The infrared detector is an R.C.A. type 7102 photomultiplier which has an S-1 photocathode. When compared with other photosurfaces, the S-1 photocathode is relatively sensitive to infrared wavelengths. Nevertheless, the quantum efficiency is low enough that liquid nitrogen cooling is required for reducing the otherwise significant thermally induced dark current.

In order to put a number on the signal to noise ratio of the infrared channel, the magnitude of a 1MHz beat frequency signal

coming through the aforementioned band pass filter (1MHz $\pm$ 200kHz) was measured and compared to the magnitude of the noise coming through this same filter when the interferometer was detuned. The result gave a figure of about 1.5 for this ratio.

Referring to Equation 3.9, the signal to noise ratio can be improved by increasing the strength of the reference laser. However, the gain must not be increased beyond the point where it can support more than one longitudinal mode. The power contained in these additional modes would add to the level of the D.C. field strength and hence to the shot noise. Furthermore, these additional modes could mix with the original one and produce unwanted frequency terms. Unless the magnitudes of these frequencies were outside the bandwidth of the photomultiplier, thereofre, such terms would serve only to impair the proper signal demodulation.

3.7 Summary

In summary, this interferometric system is a sensitive instrument capable of investigating plasma phenomena at two wavelengths either separately or simultaneously. Its other features include the following ones: 1) a spatial resolution of less than 1mm; 2) a sensitivity to the polarity of a plasma's index of refraction change; and 3) a display of plasma phenomena in real time rather than in the frequency domain. The use of the present apparatus is limited to a study of index changes which lead to beat frequency shifts of less than 250kHz.

3.8 Discharge Tubes

Since the heterodyne interferometer has been discussed, it is next necessary to describe the plasma tubes which were studied. In general, there were two basic types. They are shown in the photograph of Figure 3.7 . The pyrex tube at the top of the picture was used in the early high current (>1 amp) studies. It is 30cm long and has a 4mm bore diameter. A glass housing surrounds the small diameter inner tube to facilitate water cooling. With a water flow rate of about a liter per minute, this tube has been operated, on a 20% duty cycle (10ms "on" time, 40ms "off" time), at currents up to 50 amperes. The SCR inverter circuit which was used for modulating the current through the tube in this manner is described in Appendix II.

A tube which chronologically preceded the 30cm tube shown in Figure 3.7 but was otherwise identical to it, sustained laser action on the AII 4880Å line for a gas fill pressure of 0.1 Torr. No magnetic confinement was used. For a 20% duty cycle, the threshold current was about 10 amperes.

The majority of the measurements made during this experiment were performed on the 10cm long discharge tube shown in the lower half of Figure 3.7 . For this reason it will be described in greater detail.

Among the important physical properties of this tube are that it was made from Pyrex glass, its active discharge length is 10cm,

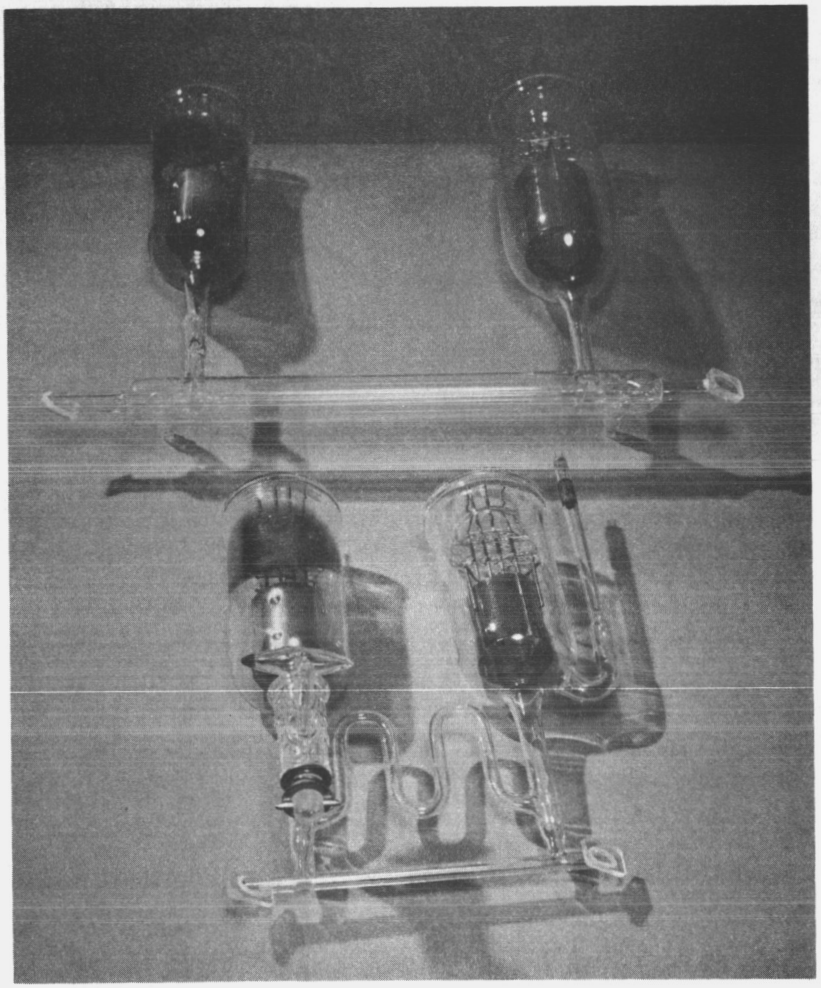

Figure 3.7 Argon Discharge Tubes

and its bore diameter is 4mm. The anode was fabricated from molybdenum. The cathode consists of an oxide-coated ribbon inside a nickel cylinder. The primary reason for using such large anode and cathode assemblies on this low current (<1 amp) discharge tube was to provide large gas reservoirs to minimize the effect of gas "clean-up". Gas "clean-up" is the condition whereby gas atoms become adsorbed to the glass and metal surfaces and are essentially lost from the discharge. This loss is evidenced by a gradual drop in the gas pressure. Additional reasons were that the large anode surface leads to a more stable discharge operation at the anode, the nickelate cathodes were readily available, and the activation and operation of the nickelate cathodes had become a routine operation in this laboratory.

The appendage on the anode housing is a Pirani tube and was used for periodically monitoring the gas pressure in the discharge tube throughout the experiment. Finally, the zig-zag shaped tube connecting the anode and cathode chambers is a pressure relief tube. Its purpose is to equalize the pressure of the gas along the discharge path being probed with the laser interferometer. The occurrence of longitudinal pressure gradients in argon tubes not equipped with relief passages has been reported[29] and argon laser tubes will not oscillate continuously without them. In all

---

*The nickelate cathodes were purchased from the General Electric Vacuum Tube Division in Owensboro, Kentucky.

instances the discharge tubes were fabricated to simulate closely argon laser tubes and were filled to pressures covering the range found suitable for such tubes.

The cleanliness of the volume and gas within the discharge tube was ensured by the following processes. First the tube was baked at 450°C under a high vacuum ($\lesssim 10^{-8}$ Torr) for 24 hours. After baking, the tube was allowed to cool. Argon gas, obtained from the Linde Company, was then introduced. Upon setting the desired pressure, the discharge tube was sealed off from the vacuum and gas handling system. Finally, a barium getter located within the tube was flashed in order to maintain a very low impurity content.

The electrical characterisitcs of the 10cm active length discharge are presented in Figure 3.8 . These voltage-current curves were measured for two typical operating pressures. The filament was run at 11 amps D.C.

Note that the voltage across the tube for a given current increases with pressure. The reason for this is that the electron drift velocity varies as the square root of the electric field to pressure ratio. Thus, in order to maintain a given current, the axial field or equivalently the voltage across the tube must be increased as the pressure increases.

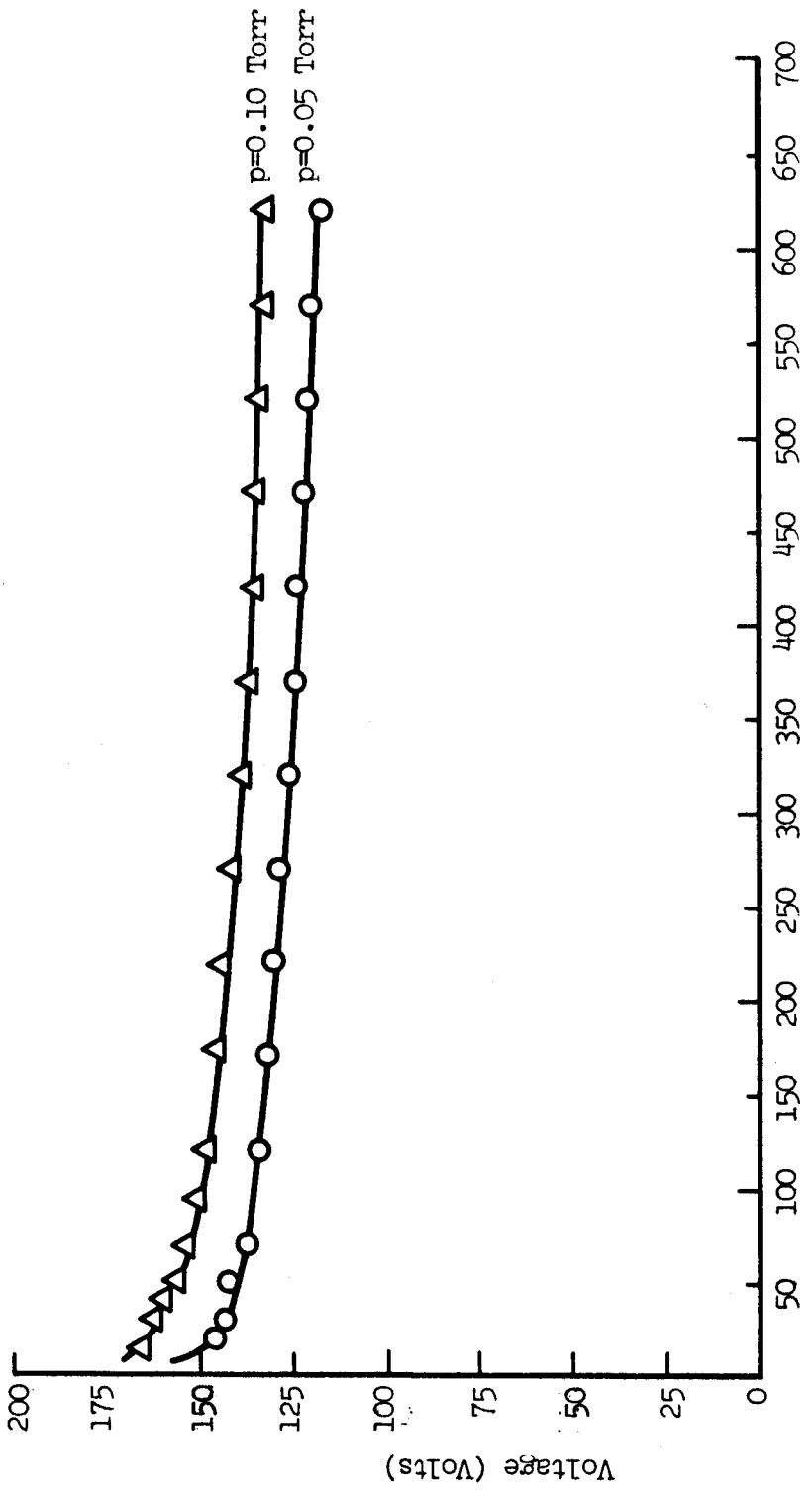

Figure 3.8 Electrical Characteristics at Two Pressures for the 10cm Long Argon Discharge Tube.

CHAPTER IV

RESULTS OF MEASUREMENTS IN ARGON

4.1 Preliminary Investigations

The initial argon studies were conducted on a 30cm long water-cooled discharge tube filled with argon at 0.1 Torr. It was felt that if the discharge current were increased sufficiently, then the primary index of refraction contribution would be due to the plasma electrons. Therefore, an attempt was made to measure the beat frequency shifts for currents in excess of 5 amperes. The technique employed was to square wave modulate the discharge current at a low duty cycle using the SCR inverter circuit. A small keep alive current ($\sim$20ma) was maintained so that the tube did not have to be relighted after each pulse.

Several facts came out of this earliest study, none of which, unfortunately, gave very much information on the argon plasma.

1. The stability of the interferometer was not severely impaired by a one liter per minute (or slower) water flow through the outer jacket of the discharge tube.

2. Since the interferometer is mounted on an iron table and because the plasma tube is located near the tungsten wire of the tuning tube, it was deemed possible that large current pulses

through the discharge might produce magnetic fields which would affect the interferometer's stability. In order to check this condition, the plasma tube was moved just outside the laser cavity. Current pulses up to 20 amps failed to produce any noticeable effect on the frequency stability.

3. The beat frequency response to the square wave current modulation had an interesting waveform. A sample trace of the visible channel's signal, taken with the feedback loop open, is shown in Figure 4.1. The appearance of the infrared channel's wave-shape was similar. Rather than follow the anticipated square wave input, these signals seem to be a superposition of a square wave with some other ramplike curve. The square-wave like nature is evidenced, for example, by the abrupt vertical jumps in the beat frequency at the leading and trailing edges of the current pulse. The magnitudes of these jumps are nearly equal and apparently relate to ionization and excitation processes occurring within the discharge.

A reasonable explanation for the presence of the ramplike function is that the current pulse provides a heat input to the walls of the discharge tube. Some of this heat is then transferred to the gas atoms which strike the walls and thereby increases their temperature. It is a good assumption that all of the gas atoms within a particular cross-section are heated uniformly if the mean distance between atom collisions is larger than or comparable to the tube radius. For argon at 0.1 Torr pressure, the mean free path is about

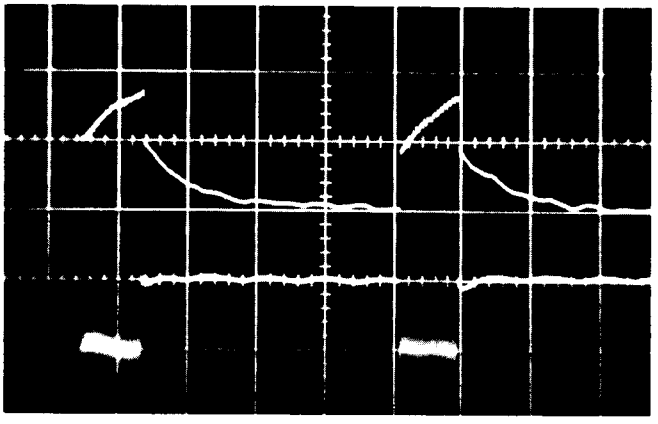

Upper Trace:
Detector Output at
+360kHz/cm.

Lower Trace:
Plasma Tube Current
Increasing Downward at
100ma/cm.

Horizontal Sweep:
10ms/cm.

Figure 4.1 Detector Output Showing Wall Heating Effect.

0.5mm. Hence, a reasonably high degree of coupling between the walls and atoms presumably exists.

As the gas temperature rises, an associated pressure increase causes some of the atoms within the active discharge to move into lower pressure regions such as the anode chamber. The net result is a slight lowering of the index of refraction of the gas being probed by the laser beams. By Equation 2.11 then, the beat frequency increases. A 300kHz shift on the visible channel corresponds to a 5 1/2% atom loss (calculated with respect to the number of atoms at 0.1 Torr and 300°K). This relatively small depletion, therefore, apparently has little effect on the index of refraction changes due to ionization and excitation since the abrupt initial and final jumps in beat frequency have nearly the same magnitude.

4. The frequency shift (measured as the magnitude of the vertical jumps) on the visible channel for currents between 0.1 and 4 amperes was approximately linear. Its magnitude, however, if attributed only to electrons led to densities almost 10 times larger than any reasonable estimate.

5. For currents in excess of several hundred milliamperes, the beat frequency shift on the infrared channel was greater than 250kHz and hence could not be measured.

In order to understand the physics behind the argon tube's index of refraction behavior, it was necessary to study a discharge operated at low currents (<1 ampere). Furthermore, since the frequency shifts

were large and the infrared channel's bandwidth was limited, it was advisable to use a shorter plasma tube. (Refer to Equation 2.11). A length of 10cm was chosen.

A 10cm discharge tube filled with argon at 0.1 Torr was used for the first run. A capacitor discharge single shot pulser provided 500 microsecond variable amplitude square wave current pulses. The circuit for this device is given in Appendix II. Its single shot feature was desirable since it minimized the amount of heat dissipated by the discharge into the laser cavity. Transient heat inputs can produce unwanted frequency instabilities. Once again, a small keep alive current was maintained.

A sample photograph showing the beat frequency response at both wavelengths to the one-shot current pulse is given in Figure 4.2. Note the linear increase in beat frequency after the initial shift. This is attributed to wall heating and was discussed earlier. Several additional observations were made in order to substantiate this hypothesis for the present situation. First, as a check on the assumption that the atoms are heated uniformly across the tube diameter, the slope of the linear rise was measured for several radial positions. As expected, the sharpness of the rise was nearly constant for a given current. Finally, one would expect that the amount of heat imparted to the tube walls would increase with current. In agreement, the slope of the rise was observed to increase slightly with current.

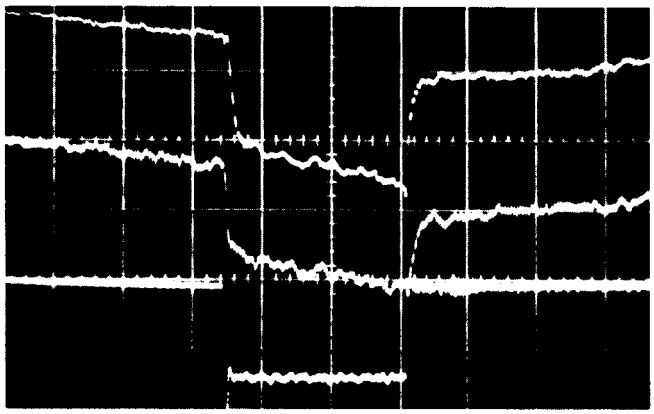

Upper Trace:
Visible Channel Output
at -73kHz/cm.

Middle Trace:
Infrared Channel Output
at -40 kHz/cm.

Lower Trace:
Current Increasing
Downward at 100ma/cm.

Horizontal Sweep:
200μsec/cm.

Figure 4.2 F.M. Detector Outputs Showing Beat Frequency Response at Two Wavelengths.

Referring to Figure 4.2 again, note that the magnitude of the square wave component in a particular waveform is readily obtained by measuring the separation between the trace segment which occurs during the pulse and a straight line drawn parallel to this segment at a distance corresponding to the very nearly equal initial and final jumps.

The measured square-wave component, beat frequency shifts at the two wavelengths are given as a function of discharge current in Figure 4.3 . These shifts were observed with the laser beams probing the center of the plasma tube. Furthermore they are absolute in nature. That is, a correction has been made for the frequency shift associated with turning off the small keep alive current.

At this point, one will recall Equation 2.11 and the results of the index of refraction calculations summarized in Table 2.6 . In terms of this information, an analysis of the data in Figure 4.3 leads one to the following conclusions.

1. The index of refraction change is not due to the ionization process alone. There are several reasons. First, the negative shift at low currents on the infrared channel would require a negative electron density. Secondly, the shifts on the visible channel at low currents are too large. For example, the shift at 65ma is 160kHz. On the basis of an ionization process, such a shift implies the formation of 1.6×10^{13} electrons per cm^3 . At 65ma, this

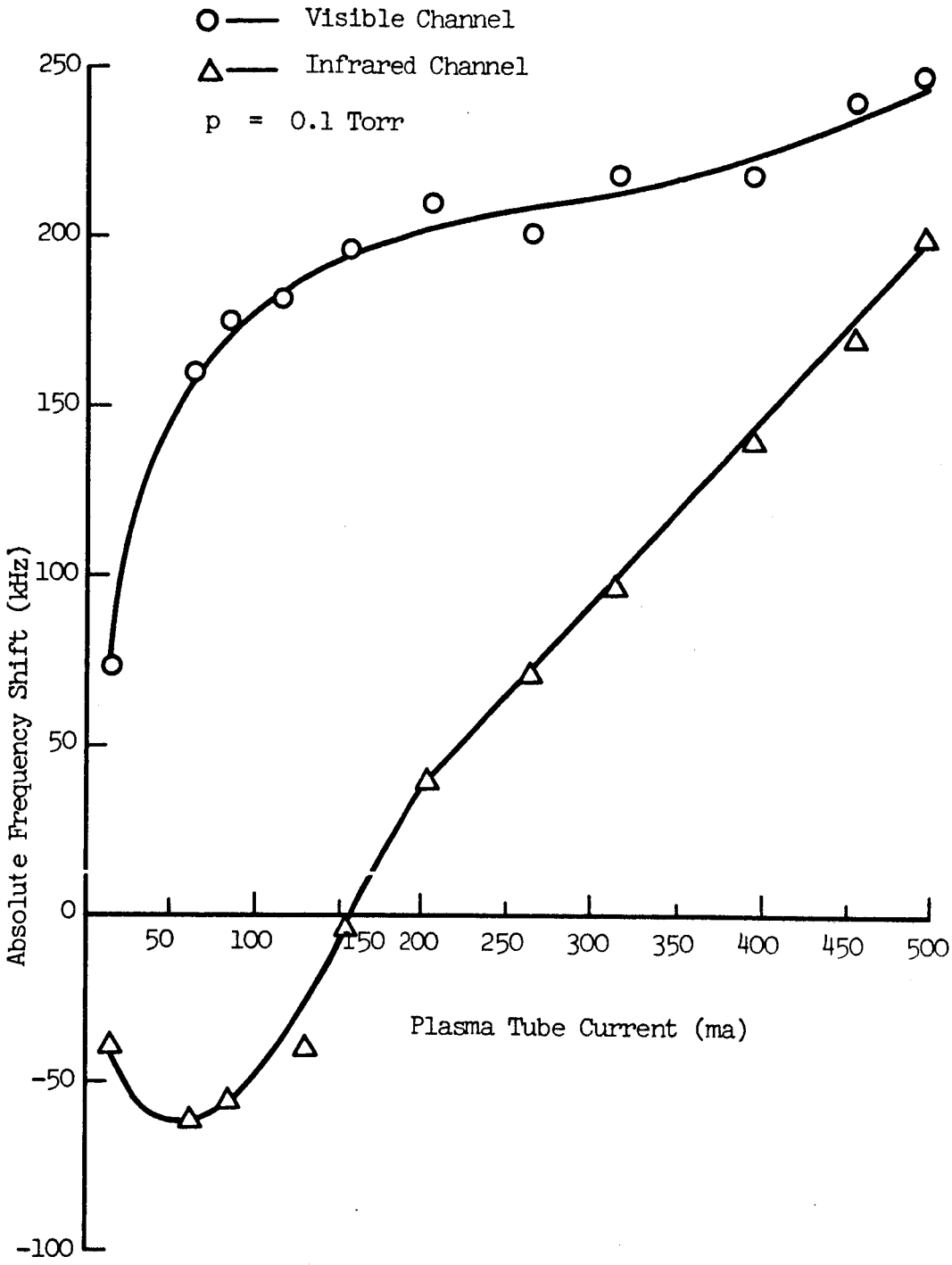

Figure 4.3 Frequency Shifts vs. Current

value is unreasonable. Finally, if the shifts were due only to ionization, the infrared shift would necessarily be about two times larger than the visible shift for a given current. Clearly the observed shift is much smaller on the infrared channel.

2. There are reports in the literature[30,31] on experiments performed with large diameter (>1cm) argon discharge tubes at pressures greater than 0.5 Torr in which a radial variation of atom density was observed. This variation was caused by a localized heating of the gas which produced a rarification of atoms at the center of the tube and a buildup at the walls. Such an effect is not dominant in the present work, however, since a depletion of atoms at the tube center would show up as a positive beat frequency shift on both the visible and infrared channels. Whereas the shift on the visible channel is consistent with an atom decrease, the infrared shift is anomolously small and in fact goes negative at low currents. Furthermore, when the discharge was probed near the wall, the frequency shifts followed the same general pattern as the results shown in Figure 4.3. If a build up of atoms actually occurred near the wall and the effect were important, a severe reduction or sign change would appear in the frequency shift behavior.

As a final note in support of the claim that ionization and radial gas density variations are not solely, if in part, responsible for the observed index of refraction changes, the results of some work done with argon by A.B. Larsen are recalled.[32]

It is an easy matter to show that the weighted frequency difference

$$\Delta\nu_W = \Delta\nu - \frac{\nu}{\nu'}\Delta\nu' \qquad (4.1)$$

can be formed to eliminate wavelength independent index of refraction changes such as those caused by gas motion. The shifts $\Delta\nu$ and $\Delta\nu'$ are the beat frequency changes at two different probe frequencies ν and ν', respectively.

Figure 4.4 shows an oscillograph made by Larsen of $\Delta\nu_W$ as a function of plasma tube current. The very non-linear response to the linear current increase clearly indicates that the remaining dependence is not a function simply of the electron density.

3. An explanation which is consistent with the qualitative nature of the frequency shifts shown in Figure 3.4 is that the index of refraction change due to metastable atoms is important. From Table 2.6 and Equation 2.11, the shift at 6328Å is positive, whereas at 11523Å, the formation of metastables would produce a negative frequency shift.

4.2 Separation of Metastable and Electron Densities

If we assume that the index of refraction change of the argon discharge is due principally to the ionization process and to the formation of metastable atoms, we may write from Equation 2.11 that

$$\Delta\nu_1 = -\nu_1 \frac{\ell}{L}\left[\Delta n_{\text{ionization}}(\nu_1) + \Delta n_1(\nu_1)\right], \qquad (4.2a)$$

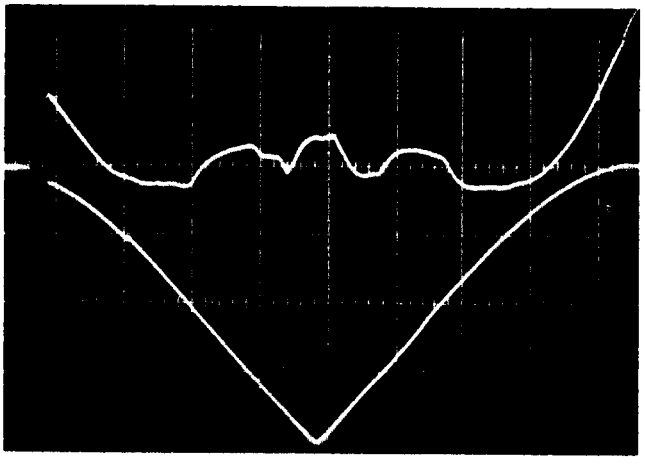

Upper Trace:
Combined Output at
40kHz/cm.

Lower Trace:
Discharge Current at
20ma/cm.
(Increasing Downward)

Tube Diameter: 1.6cm
Pressure: 0.1 Torr.

Figure 4.4 Oscillograph of Combined Output vs. Current After Larsen.[32]

and $$\Delta\nu_2 = -\nu_2 \frac{\ell}{L} [\Delta n_{ionization}(\nu_2)+\Delta n_1(\nu_2)] , \qquad (4.2b)$$

where $\Delta\nu_1$ and $\Delta\nu_2$ are the beat frequency shifts on the visible ($6328\mathring{A}$) and infrared ($11523\mathring{A}$) channels resepctively. The validity of neglecting a possible radial gas density variation is checked later by making measurements at different pressures. The present necessity for considering only two variables is a direct consequence of operating at just two wavelengths. Theoretically a third equation expressing conservation of particles could be written. However, this equation involves integrals over radial density profiles. In short, the whole problem becomes extremely complicated.

Upon substituting for $\Delta n_{ionization}$ and Δn_1 from Table 2.6, Equations 4.2a and 4.2b can be solved for the electron and metastable densities, The result is that

$$N_e = \frac{L}{\ell} 4.44\times10^6(0.78\Delta\nu_1 + \Delta\nu_2) , \qquad (4.3a)$$

and $$N_1 = \frac{L}{\ell} 2.06\times10^6(1.74\Delta\nu_1 - \Delta\nu_2) . \qquad (4.3b)$$

When values for $\Delta\nu_1$ and $\Delta\nu_2$ from Figure 4.3 and from measurements made at other radial positions are substituted into Equations 4.3a and 4.3b, the curves shown in Figures 4.5 and 4.6 are obtained. The symbol "r" designates the vertical distance from the center of the tube to the position probed by the beams.

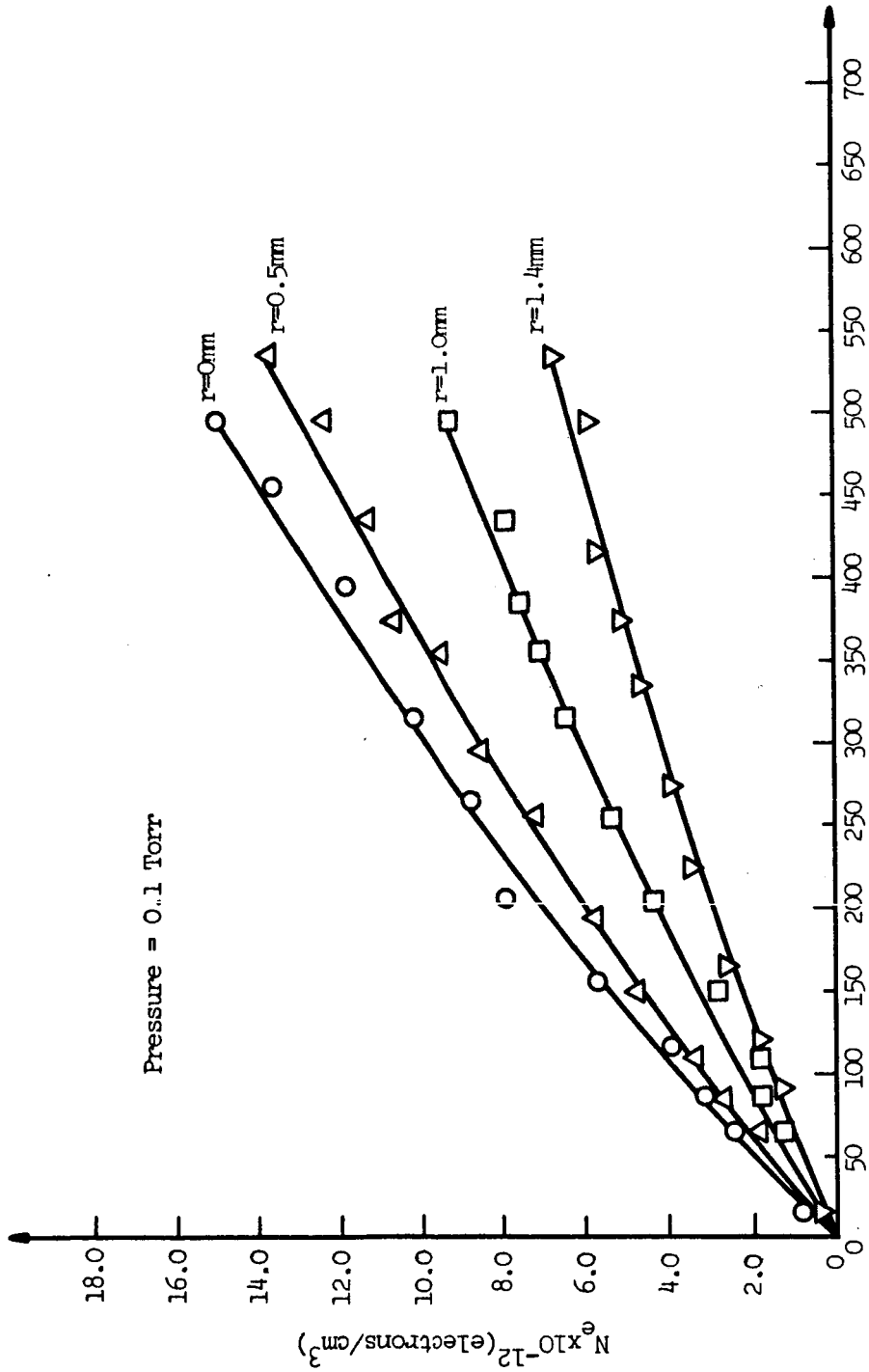

Figure 4.5 Electron Density vs. Current.

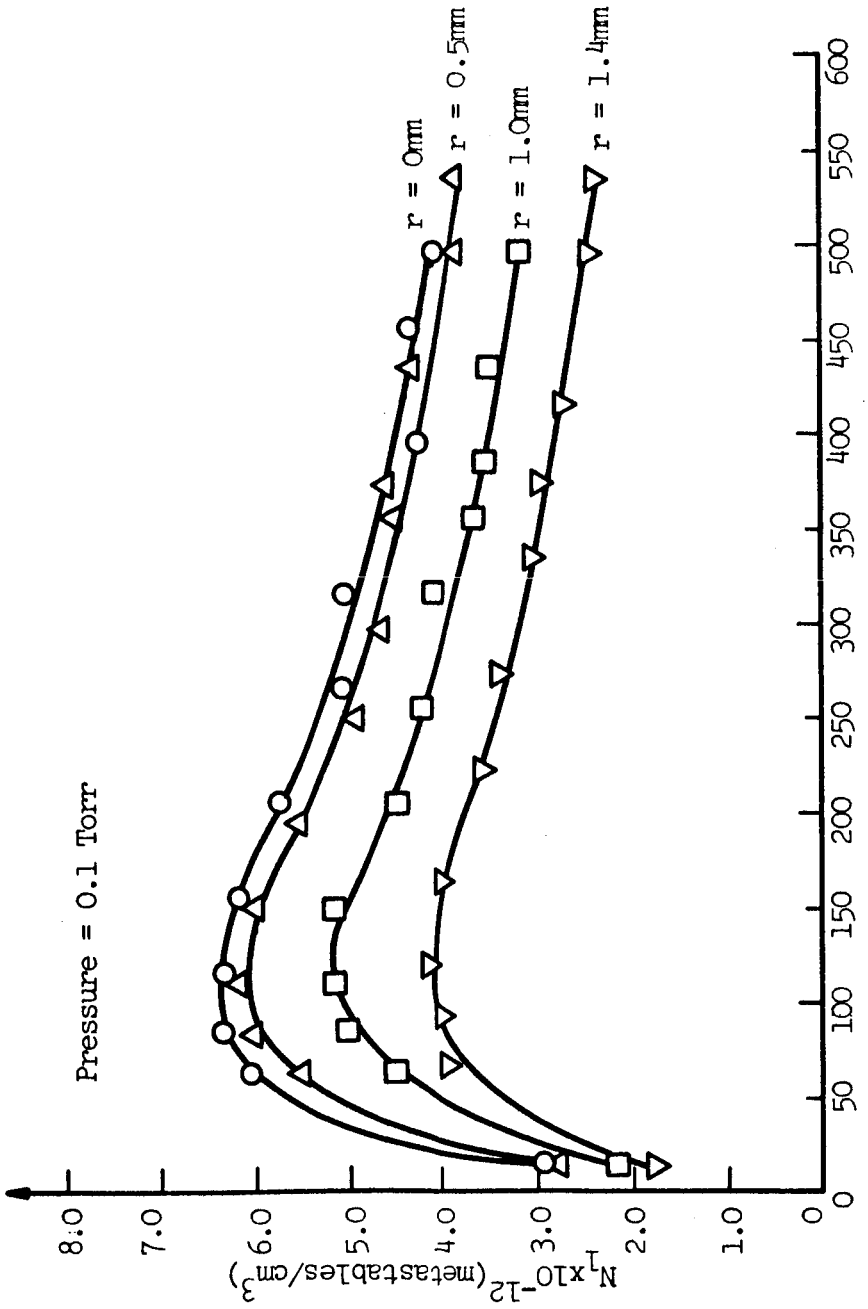

Figure 4.6 Total Metastable Density vs. Current.

A positive value for "r" indicates that the region probed was above the tube center. The method for moving the discharge tube involved the use of two precision micrometer stages, shown previously in Figure 3.3. These micrometers were calibrated to within 0.1mm. Tube center was determined by splitting the difference between micrometer readings taken when the laser beams were immediately adjacent first to one wall of the discharge tube, then to the opposite wall. The position $r = 1.4$ represents the furthest distance away from center at which measurements could be made. Beyond this value, the laser beams went out due to excessive diffraction losses introduced by the tube walls.

Referring to Figure 4.5, note that the curves for the electron density pass through zero as required and are nearly straight lines. The slight sublinear (slower than linear) rise is discussed as follows. In terms of the electron mobility μ^- and axial electric field E, the current density J through the discharge is

$$J = eN_e\mu^-E \ . \qquad (4.4)$$

Further the mobility is[33]

$$\mu^- = \left(\frac{\pi eL_e}{2mE}\right)^{1/2} \ , \qquad (4.5)$$

where L_e is the mean distance between electron-atom collisions. If Equations 4.4 and 4.5 are now combined, the solution for N_e is

$$N_e = \left(\frac{2m}{\pi e^3 L_e E}\right)^{1/2} J \ . \qquad (4.6)$$

The variations of L_e and E with current are known. That is, since L_e increases with a decrease in electron temperature,[34] and because the electron temperature in a discharge similar to the present one has been observed to decrease with current,[35] the mean-free path of electrons increases with current. From Figure 3.7, the tube voltage or equivalently the axial field, decreases slightly with current. (Note that this decrease in E is responsible for the decrease in electron temperature mentioned above).

Thus, the coefficient in Equation 4.6 is a function of current but the direction of this dependence is not inherently obvious. The present experimental curves, however, indicate that the increase in L_e is dominant.

The results obtained for electron and metastable densities were not checked by any additional method. Normally a simple Langmuir probe measurement could be made to readily test the electron density values. In this case, however, due to the small bore diameter of the discharge, the presence of such a probe would almost certainly "disturb" the plasma to an appreciable extent. Measurements with shielded double probes could probably have been made, but the additional difficulties involved put this undertaking outside the scope of the present project. In addition, the spatial resolution of probes is limited to several millimeters.

In partial support of the present data, it is possible to make a rough comparison with some results obtained at the Bell Telephone

Laboratories.[36] Using shielded double probes, the electron density at low currents in a narrow-bore discharge was measured to be a sublinear function of current for fill pressures of less than 2 Torr. The magnitude of the current density was of the same order as that obtained in the present experiment. Finally, the population of the $1s_5$ metastable level was measured by the so-called Ladenburg-Reiche technique. Interestingly, the density was observed to increase rapidly to a maximum value, then fall off gradually. No quantitative comparison can be made with the present data, however, since the tube diameters and fill pressures were different for the two experiments.

4.3 Measurements at Other Fill Pressures

In order to obtain additional information about the argon plasma and to further substantiate the assumptions made in the analysis, measurements were made at two other fill pressures. The results for argon at 0.05 Torr and 0.3 Torr are given in Figures 4.7 - 4.10 .

Referring to Figures 4.7 and 4.9, note that the electron density curves extend through the origin. The significance of this fact is that a possible shift in the beat frequency caused by radial atom motion is not dominant. For example, at the tube center, a net outflux of atoms would cause both the visible and infrared shifts to be overly large. By Equation 4.2a therefore, the calculated value for electron density would be excessive. Hence, the

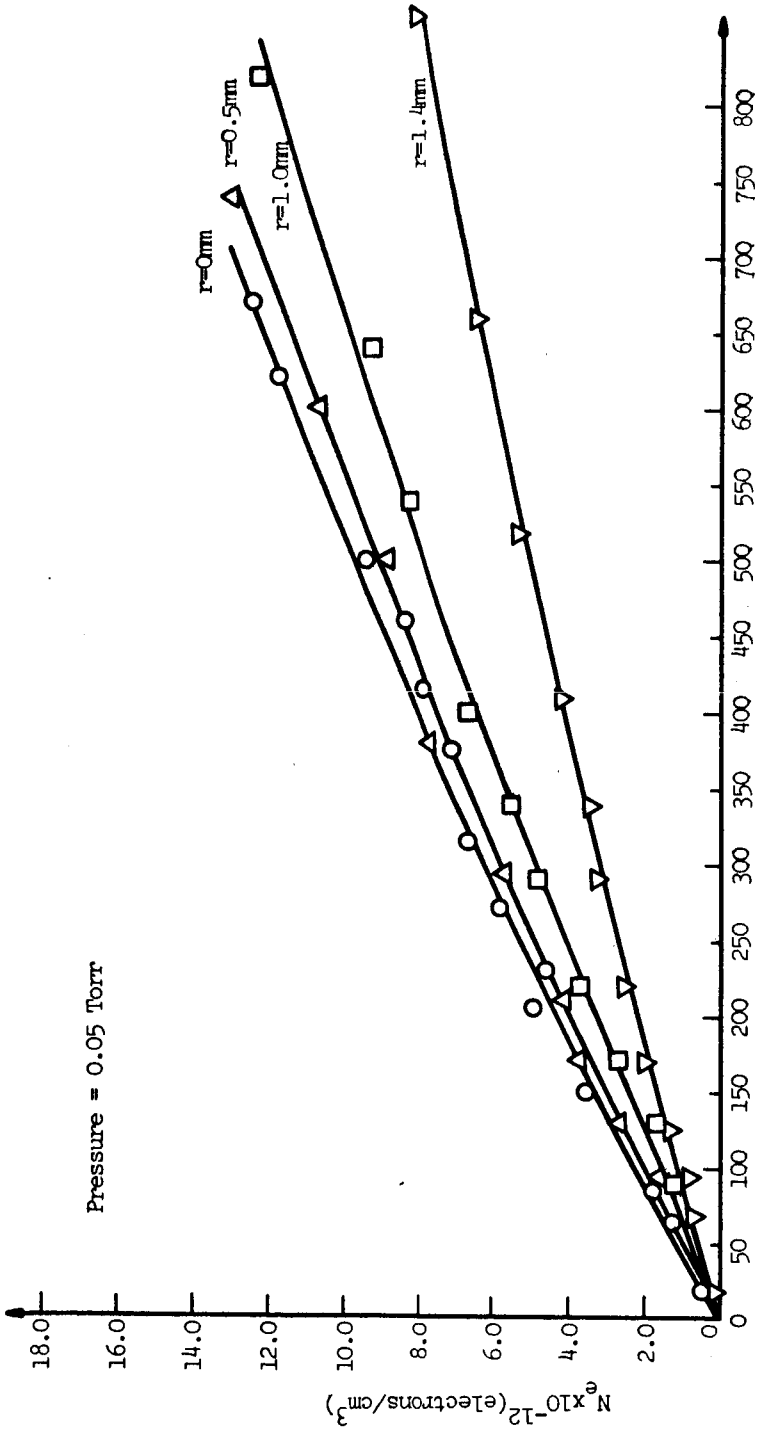

Figure 4.7 Electron Density vs. Current for Argon at 0.05 Torr.

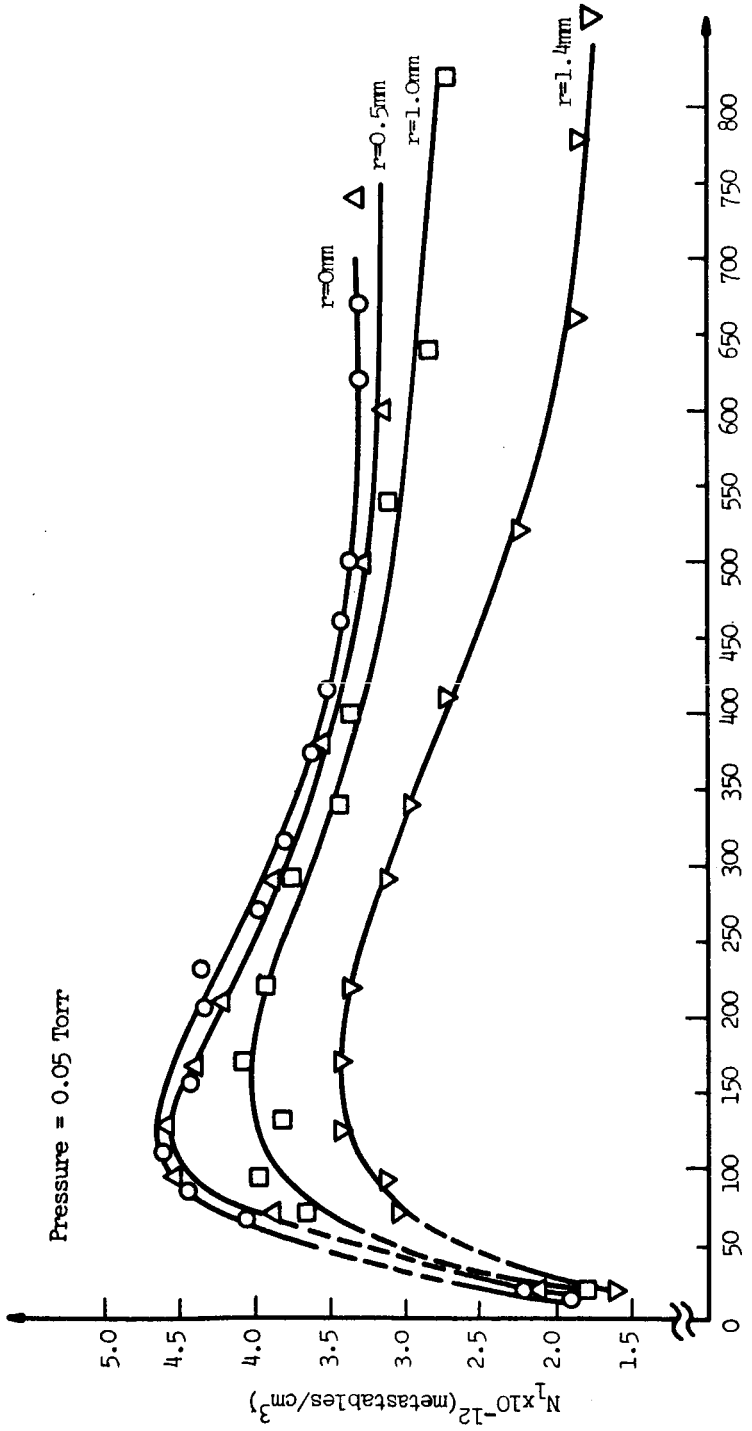

Figure 4.8 Total Metastable Density vs. Current for Argon at 0.05 Torr.

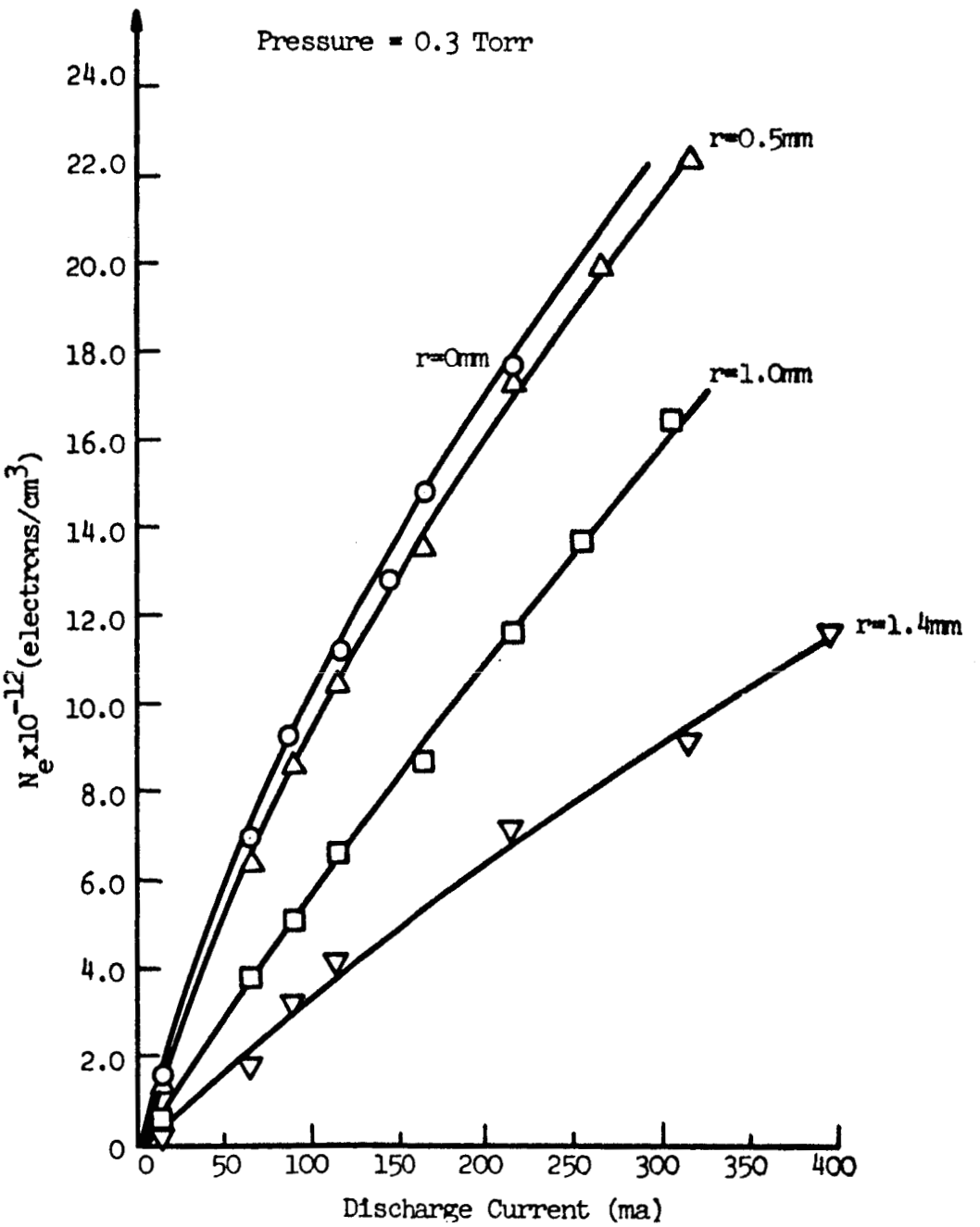

Figure 4.9 Electron Density vs. Current for Argon at 0.3 Torr.

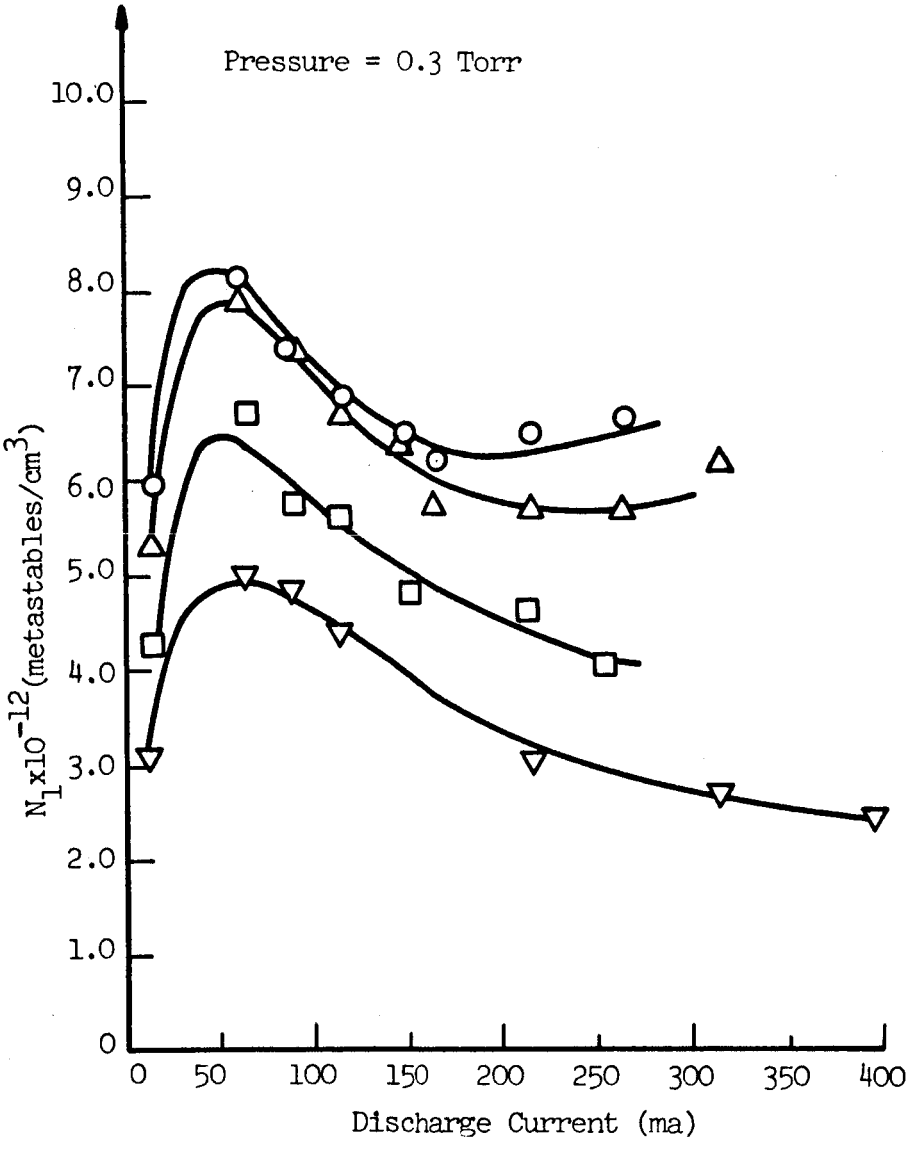

Figure 4.10 Total Metastable Density vs. Current for Argon at 0.3 Torr.

extrapolated density plot would intercept the vertical axis at some value above zero.

The electron density plots for these pressures are also slightly sublinear with current. In this regard, it can be pointed out that the plots would be even more sublinear if gas motion were significant and a correction were made for it. This is because the magnitude of the radial pumping effect would increase with current if it changed at all.

Thus far, little has been said about the nature of the metastable atom curves. This subject will be discussed in the following section.

4.4 Processes Involving Metastable Levels

An attempt to explain the appearance of the observed current and pressure dependence of the metastable density requires one to write a rate equation for the metastable states. To aid in writing such an equation, the various processes which produce and destroy the 1s levels are listed below.

1. Production:
   a) Electron collisions excite ground state atoms into metastable levels.
   b) Atoms in higher-lying excited states lose energy by radiating a photon of the proper frequency and become metastable.

c) Atoms in their normal state collide with the metastable atoms in a particular 1s level to produce metastable atoms in any of the other three 1s levels. Although this collisional mixing process does not lead to a net increase in the total number of metastable atoms, it is an important mechanism for balancing the density of atoms in one of the metastable states relative to the densities in the other three states. The presence of these near resonance atom-atom collisions was mentioned previously in Section 2.4.

2. Destruction:

a) Metastable atoms diffuse to the walls.

b) A metastable atom can collide with a neutral atom and be excited to a radiating state.[37]

c) Electron collisions can de-excite metastable atoms.

d) At high pressures, particularly, three body destruction can be important in which two neutrals collide with a metastable.[37]

e) Two metastable atoms can collide and become ionized.[37]

f) Resonance transitions from the $1s_2$ and $1s_4$ levels exist, however this radiation is imprisoned. For a gas density of 0.1 Torr,

the characteristic distance which a photon from one of these levels can travel before it is re-absorbed is on the order of 10^{-3}cm. Furthermore, the results of a rough calculation demonstrated that this radiation is heavily trapped for all radial positions in the discharge tube which are not immediately adjacent to the enclosing walls.

g) Metastable atoms could lose energy in collisions with ions.

If the above processes are now expressed as an equation, the rate of change of the total metastable density becomes

$$\frac{dN_1}{dt} = \langle\sigma v\rangle_{eo} N_e N_o + D\nabla^2 N_1 - \langle\sigma v\rangle_{lo} N_1 N_o + \cdot$$

$$\cdot + -\langle\sigma v\rangle_{el} N_e N_1 - SN_o^2 N_1 - \alpha N_1^2 - A_1 N_1 \ . \qquad (4.7)$$

The first term on the R.H.S. of Equation 4.7 represents the two production processes listed above, with $\langle\sigma v\rangle_{eo}$ the cross section for electron-atom collisions. The remaining terms represent the various destruction processes listed above, where D is the metastable diffusion constant, $\langle\sigma v\rangle_{lo}$ is the metastable-atom collisional cross section, $\langle\sigma v\rangle_{el}$ is associated with electron de-excitation, S is the coefficient for three-body destruction, α is the ionization coefficient, and finally, A_1 is the total probability for transitions from the metastable levels. The loss of metastables

by ion collisions is neglected since the relative atom-ion velocity is assumed to be small. Equation 4.7 can be solved for N_1 in the steady state $(\frac{dN_1}{dt} = 0)$ with the result that

$$N_1 = \frac{\langle\sigma v\rangle_{eo} N_e N_o}{-D \frac{\nabla^2 N_1}{N_1} + \langle\sigma v\rangle_{1o} N_o + \langle\sigma v\rangle_{el} N_e + S N_o^2 + \alpha N_1 + A_1} \qquad (4.8)$$

For the purpose of facilitating an interpretation of the data using Equation 4.8, N_1 is plotted versus N_e for the three pressures in Figures 4.11-4.13. Initially, for all three pressures, N_1 increases rapidly with N_e. Therefore, the destruction of metastable atoms is by diffusion to the walls. If electron de-excitation were dominant, a strong electron density dependence would not be observed. The remaining destruction terms are neglected on the basis of a general knowledge that their effect is small in a discharge of this type.

In the portion of the N_1 vs. N_e curves under discussion, the diffusion term for a particular current and pressure is constant. This is due to the fact that the radial profile of N_1 follows a Bessel function. For example, N_1 is plotted versus radial position for two presssures in Figure 4.14.

On the basis that the diffusion term is constant, N_1 should increase with N_o or pressure. Indeed the observed metastable density is larger for the higher pressure, however the dependence is not linear. The reason for this nonlinearity is that the cross

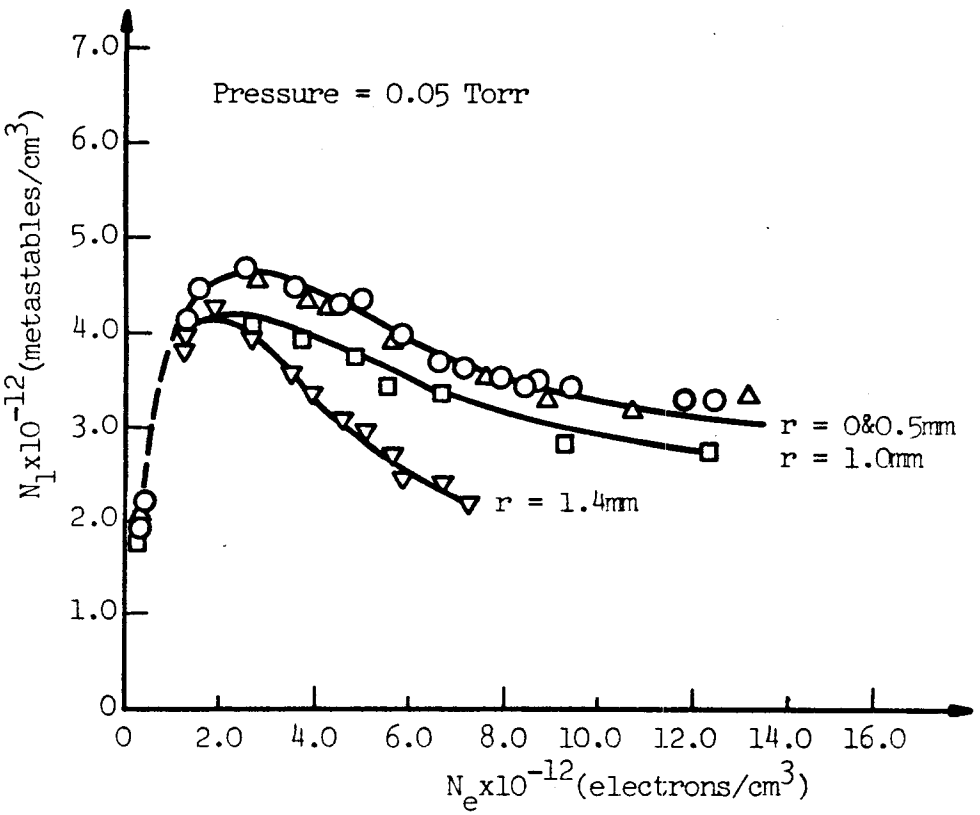

Figure 4.11 Metastable Density vs. Electron Density for 0.05 Torr.

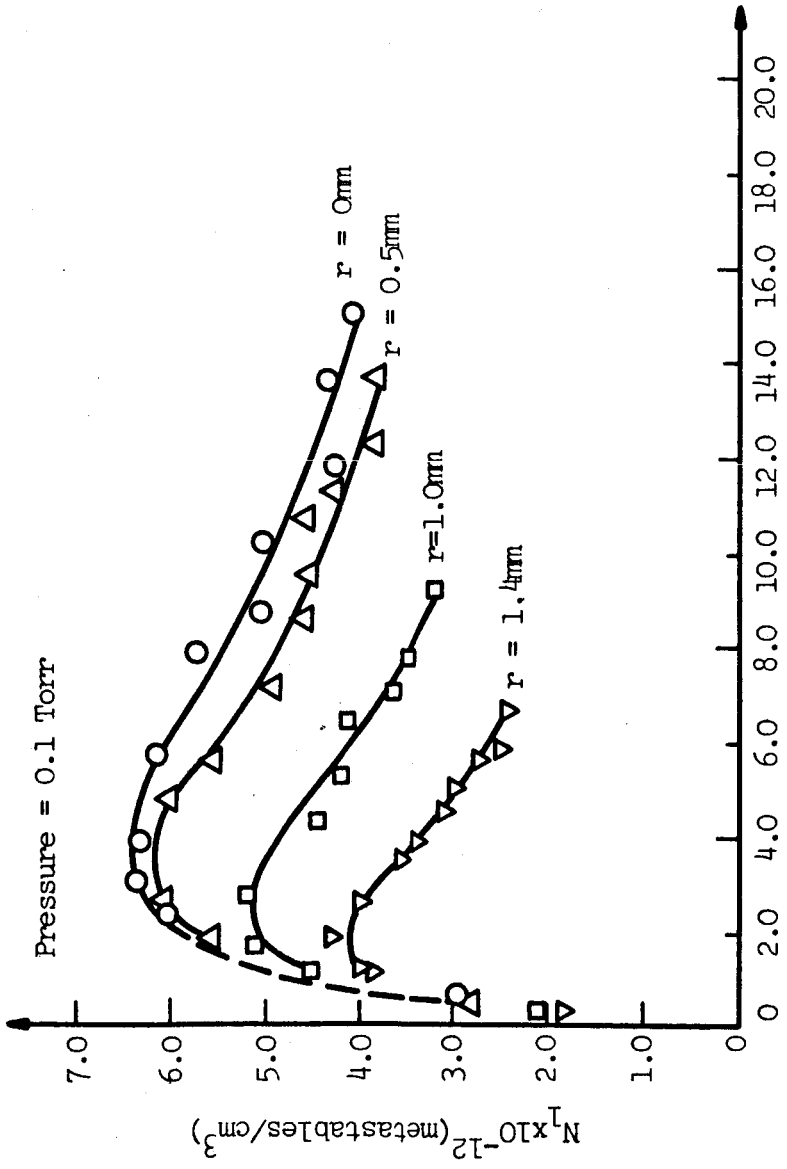

Figure 4.12 Metastable Density vs. Electron Density for 0.1 Torr.

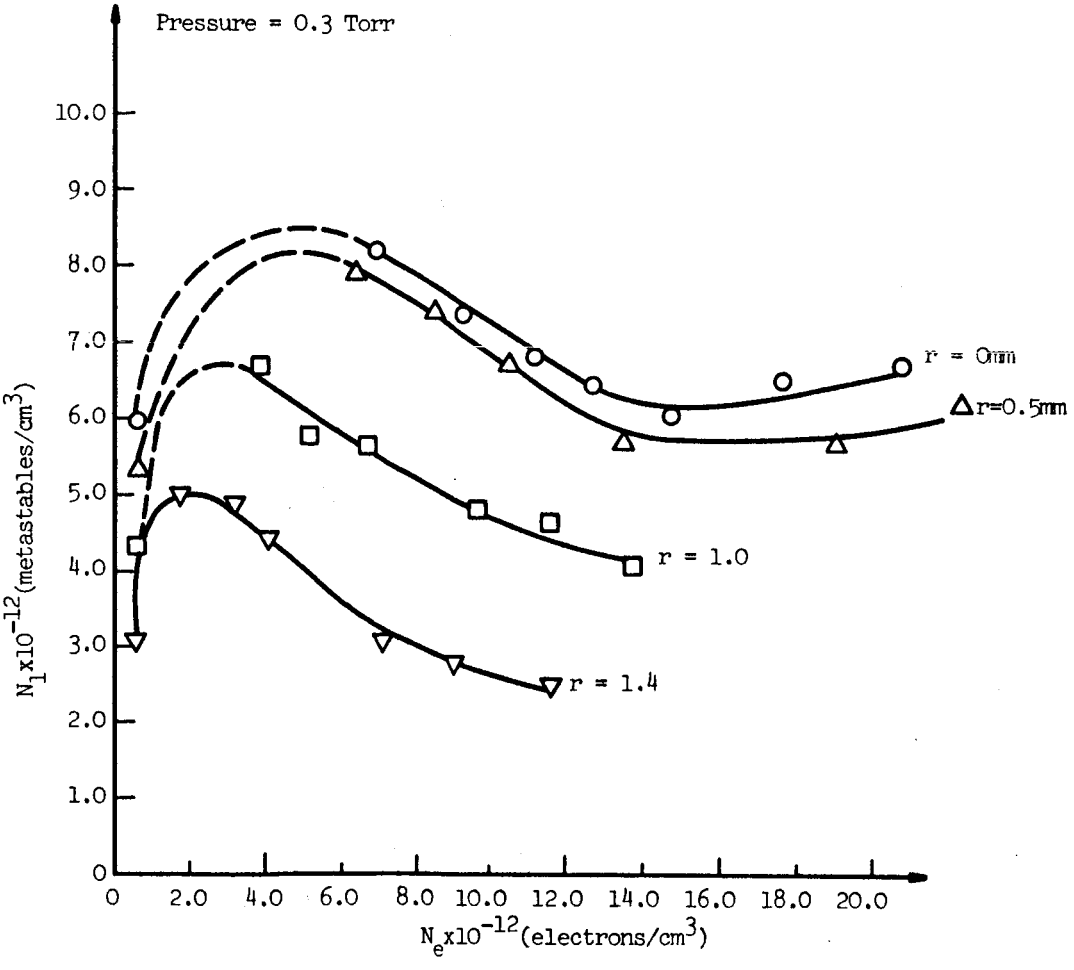

Figure 4.13 Metastable Density vs. Electron Density for 0.3 Torr.

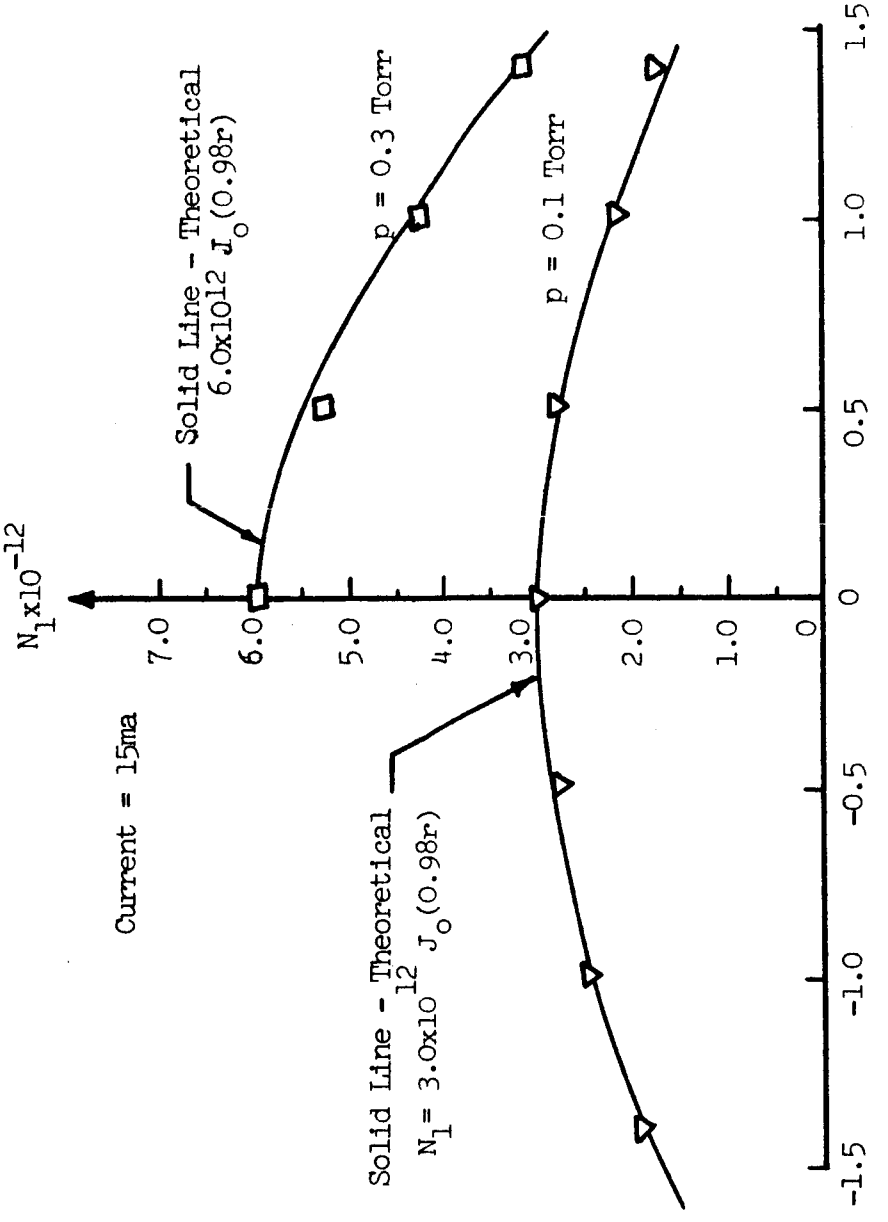

Figure 4.14 Radial Profile of Metastable Density at Low Current.

section $\langle\sigma v\rangle_{eo}$ decreases because of a decrease in electron temperature as the pressure is increased. That is, as the pressure increases, the mean free path of the electrons becomes smaller and the electron temperature decreases.

The possibility of obtaining values for the electron excitation cross-section $\langle\sigma v\rangle_{eo}$ at the various pressures was considered. For the diffusion controlled region being discussed, Equation 4.8 simplifies to the following expression

$$N_1 = \frac{\langle\sigma v\rangle_{eo} N_e N_o}{-\tilde{D}\frac{\nabla^2 N_1}{N_1}} \quad . \tag{4.9}$$

If the diffusion constant D for the metastable atoms were known, it would be a straightforward problem to solve for $\langle\sigma v\rangle_{eo}$ using the information in Figure 4.14 to obtain $\frac{\nabla^2 N_1}{N_1}$. However, a value for the diffusion coefficient of argon metastable atoms is not available and it was not possible to measure this quantity using these experimental techniques.

Referring again to Figures 4.11 - 4.13, one will observe that the metastable atom curves reach a peak and then decrease slightly as N_e increases. It is believed that these negative slope regions occur where electron de-excitation is important. The appropriate form of Equation 4.8 for these regions, therefore, is

$$N_1 = \frac{\langle\sigma v\rangle_{eo} N_e N_o}{\langle\sigma v\rangle_{el} N_e - \frac{D\nabla^2 N_1}{N_1}} \qquad (4.10)$$

The "loss" terms due to atom-atom collisions, three body destruction, metastable ionization, and radiation have been neglected. When the radial profile of N_1 was plotted for a value of current in the region under consideration, the experimental points once again followed a Bessel function. Hence, the diffusion term remains constant.

The existence of the fall-off in the magnitude of N_1 is explained by the fact that the electron temperature and therefore $\langle\sigma v\rangle_{eo}$ decreases as N_e increases. The reason for the decrease in T_e with electron density is that the axial electric field in the discharge tube falls off with an increase in current. (Refer to the V-I characteristics given in Figure 3.8). The cross-section $\langle\sigma v\rangle_{el}$ will also decrease as T_e decreases. However, $\langle\sigma v\rangle_{el}$ decreases more slowly than $\langle\sigma v\rangle_{eo}$. The reason for this is that the electron excitation process identified by $\langle\sigma v\rangle_{eo}$ is a threshold reaction. That is, only electrons with energies in the tail of the energy distribution are involved. On the other hand, the destruction reaction described by the cross section $\langle\sigma v\rangle_{el}$ takes place regardless of the electron's energy.

For electron densities beyond 10^{13} cm^{-3} the curves begin to

level off or even increase slightly. From Equation 4.10, N_1 will be independent of N_e if destruction by electron collision dominates and the electron temperature becomes constant. Referring to Figure 3.8, the discharge tube voltage for currents in this region is nearly constant so that T_e is indeed expected to be uniform.

It is interesting to note that N_1 decreases more rapidly at radial positions close to the tube walls. A reasonable explanation for this fact involves radiation trapping. It is known from quantum mechanical selection rules that some of the 2p and 3p excited states (see Figure 2.4) in argon are radiatively connected to the $1p_o$ ground state as well as the 1s metastable levels. Also, for the conditions of this experiment, the resonance radiation from the 2p and 3p excited states to the ground state was trapped, at least for radial positions near the tube center. Thus, for regions near the center, these excited levels would have a much higher probability of decaying to the metastable levels than to the ground state. Near the edges of the tube, however, the radiation trapping is less pronounced so that fewer of these excited levels would decay to the metastable states. Consequently, the magnitude of N_1 would be smaller near the walls as observed.

Finally, one may note that the entire family of radial curves have a similar shape and that the magnitude of the separation between the curves which correspond to different radial positions

generally increases with pressure. The reason for this occurrence is not understood. It is feasible that radial gas motion would lead to this result. However, the possible presence of gas motion is inconsistent with observations described previously in this paper.

In summary, the behavior of the metastable density with current and radial position is quite complicated. At low electron densities, diffusion appears to dominate. Beyond this diffusion-controlled region, electron de-excitation increases in importance. The separation in the N_1 vs. N_e for various radial positions seems to be caused in part, at least, by radiation trapping.

4.5 Electron Distribution

Figure 4.15 shows the radial distribution of electrons for the three pressures. This data indicates that the electron density becomes more uniform across the tube as the pressure decreases. The criterion which determines whether the motion of electrons toward the wall is by free fall or ambipolar diffusion is the magnitude of the ion mean free path, L_p, compared to the tube radius.[38] If $L_p >> R$, there are few collisions between ions and atoms. Hence each ion in the discharge starts from rest or with some initial velocity and falls to the walls through a static electric field which is maintained by the balance of electron and ion charges. In the analysis of this free fall situation, the electron density is assumed to vary exponentially with the radial potential distribution and is given by[39]

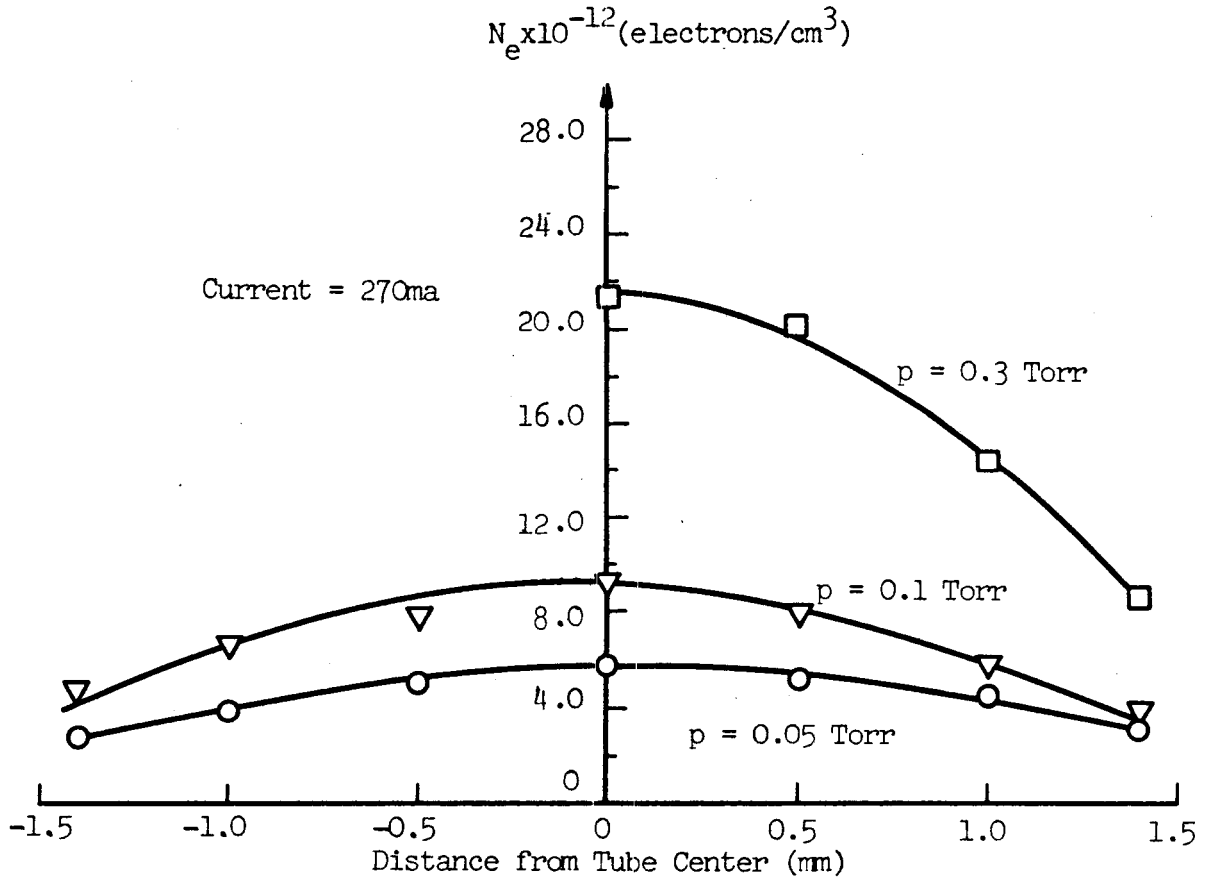

Figure 4.15 Experimental Radial Electron Distribution vs. Pressure.

$$N_e(r) = N_{eo}\exp[-1.155(1-\sqrt{1-(\frac{r}{R})^2})] \ , \qquad (4.9)$$

where N_{eo} is the electron density at the tube center.

When $L_p << R$, the motion of the ions toward the walls is no longer unimpeded. The ions must now proceed by diffusion. Further, the nature of this diffusion depends on the presence of the plasma electrons. Since the electron diffusion coefficient is much larger than that of the ions, the electrons attempt to diffuse more rapidly than the ions toward regions of lower concentration. However, their motion is impeded by the space charge field thereby created. This same field, though, has the opposite effect on the ions and causes them to diffuse faster than if the electrons were absent. The net result of this interaction is that the charged particles move with the same velocity. Thus, the flow of particles is independent of the charge polarity and is termed "ambipolar."

At 0.1 Torr, L_p was calculated to be 0.7mm . To obtain L_p at the other pressures, the scaling goes inversely with pressure. Hence, according to the theory, the present condition is midway between the two extremes. An attempt to fit the free fall density distribution (Equation 4.9) to the experimental points for 0.1 Torr failed since the theoretical curve fell off too slowly with increasing r .

If on the other hand ambipolar diffusion is important, the

following analysis applies. Assuming that electrons are produced by the process of electron impact and that electron-ion recombination is negligible compared to ambipolar diffusion, the time rate of change of the electron density is

$$\frac{dN_e}{dt} = \gamma N_e + D_a \nabla^2 N_e \qquad (4.10)$$

where γ is the number of ionizing collisions per second per electron. The quantity D_a is the ambipolar diffusion constant and is given further as

$$D_a = \frac{kT_e}{e} \mu^+ \qquad (4.11)$$

where T_e is the electron temperature and μ^+ is the mobility of the ion in a background of neutrals. The steady state solution of Equation 4.10 gives that the radial electron density distribution is

$$N_e(r) = AJ_o[(\sqrt{\frac{\gamma}{D_a}})r] \ , \qquad (4.12)$$

where $A = \frac{N_{eo}}{J_o(0)}$.

The extent to which the measured electron densities for a pressure of 0.1 Torr follow a Bessel function is demonstrated in Figure 4.16. The solid line drawn through these data points is the Bessel function $N_e(r) = 8.6 \times 10^{12} J_o(1.08r)$. It will be noted that this curve was fitted about a center line displaced 0.1mm to the left of the presumed tube center. The cause of this slight

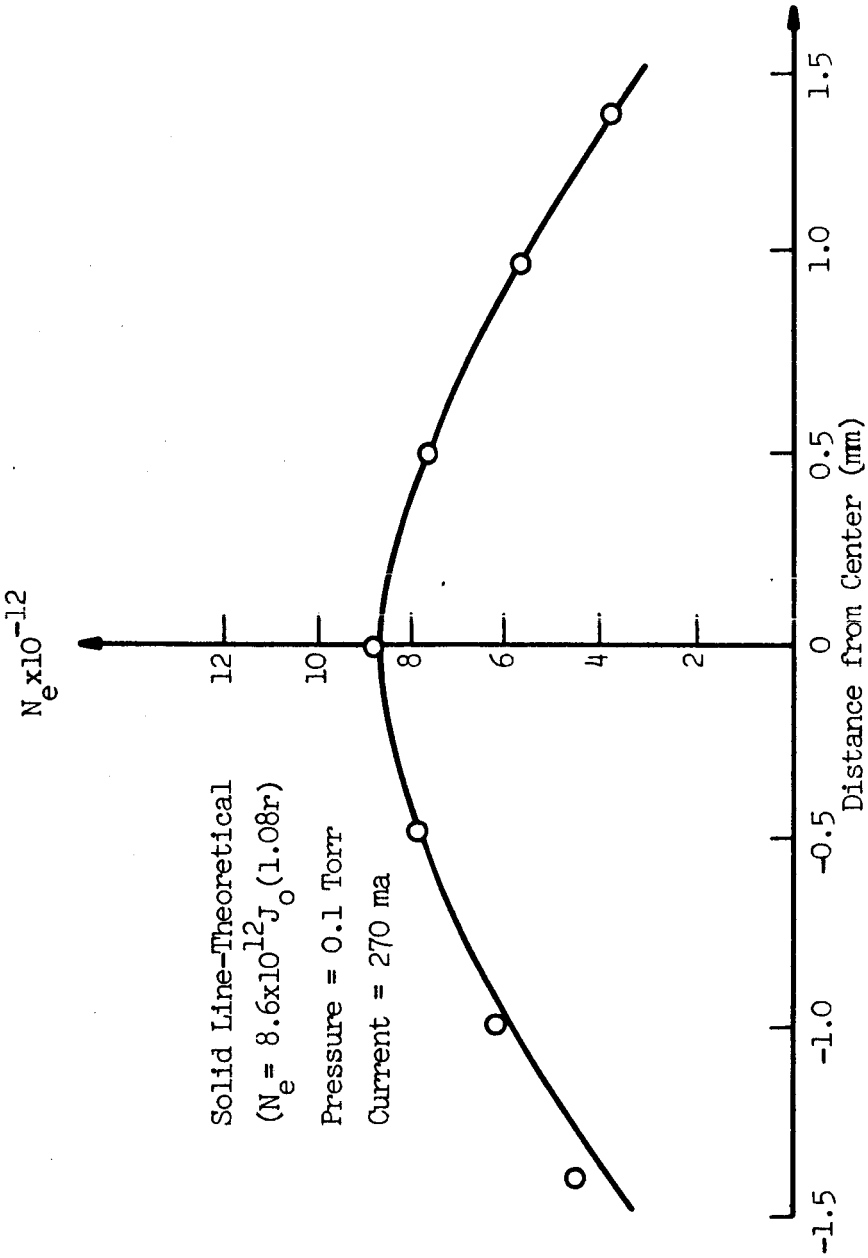

Figure 4.16 Theoretical and Experimental Values of Electron Density vs. Radius.

displacement in the points is more than likely due to a small error in the location of the tube center. (In Figure 4.15, the data for p = 0.05 Torr are displaced slightly to the right).

If the experimentally observed Bessel function argument, 1.08 is now equated to $\sqrt{\frac{\gamma}{D_a}}$, a value for γ can be obtained. Assuming an electron temperature of 40,000°K (an estimate based on values given for narrow-bore argon plasmas)[39,40] and a value of μ^+ = 1.5 cm^2/volt-sec. (obtained from Basic Data of Plasma Physics),[41] the value of γ is determined to be $\gamma = 2.3 \times 10^3$ sec^{-1}. A value for γ was not found in a search of the literature. Therefore a check on the present value is not available.

CHAPTER V

SUMMARY AND SUGGESTIONS FOR FUTURE WORK

In summary, the spatially resolved index of refraction of a 4mm bore by 10cm long argon discharge tube has been investigated with a dual wavelength heterodyne interferometer. Measurements were made at pressures of 0.05 Torr, 0.1 Torr, and 0.3 Torr for discharge currents of less than one ampere. The index of refraction changes at the two probe wavelengths (λ = 6328 Å and λ = 11523 Å) caused by a change in discharge current have been attributed primarily to the production of plasma electrons and metastable atoms. The contribution from a possible radial gas motion was not observed. Thus, equations were written for the electron and metastable densities in terms of the observed index change at the two probe wavelengths. The resulting electron density curves extended through the origin and were slightly sublinear functions of current. The curves of the total metastable atom density vs. current typically rose sharply, reached a maximum, then fell off gradually toward some level or sometimes rose again very slightly. Finally, the radial distribution of electrons was studied in the 0.1 Torr discharge for a current of 270ma. By the shape of the experimental profile, the dominant electron loss process was confirmed to be ambipolar diffusion rather than free fall to the walls.

The suggestions for future work fall into three general cate-

gories: improvements in the heterodyne interferometer; additional argon studies; and the investigation of other gases or gas mixtures.

The major difficulty with the present heterodyne interferometer is the limited bandwidth on the infrared channel. One method for improving this condition would be to increase the signal-to-noise ratio at this wavelength. This would involve either the use of a more sensitive detector or offsetting the geometrical length of the reference laser cavity with respect to the signal laser cavity. This would allow multimode operation and hence permit one to utilize the maximum power available in a particular longitudinal mode. The purpose of using different length cavities is to insure that the unwanted beat frequencies between the various modes are outside the range of the electronics.

If the signal-to-noise ratio at the infrared wavelength can not be improved significantly, an improved demodulation scheme is required. One alternative would be to improve the FM detector so that it would be even less susceptible to noise. Using the present detector, a possible solution might be to increase the bandwidth of the filter located at its input and allow signals over a wider frequency range to enter. Following the detector, then, a lock-in amplifier could be used to detect just that portion of the output which is synchronous with the modulated plasma tube current. This scheme assumes, of course, that the present detector will respond properly to a signal accompanied by additional noise. For oscillo-

graphic observation the band pass filter has already been increased as much as possible.

In addition to increasing the system bandwidth, the possibility of operating at an additional wavelength should be considered. The practical difficulties of operating at more than two wavelengths simultaneously would be unreasonable. However, a run could first be made, for example, at the two wavelengths A and B, followed by a second run at wavelengths A and C. Wavelength A is kept common to both runs and hence would act as a check on the uniformity of the experimental conditions. One possible three wavelength system would be to utilize the 3.39μ, 11523Å, and 6328Å neon transitions keeping the 11523Å, wavelength common. The 3.39μ laser line is suggested since this transition has a very high gain. The problems associated with using the 3.39μ wavelength include detection difficulties and the fact that the change in the mode pulling effect (i.e., the non-linearity between the output and cavity frequencies of the laser) will introduce and 8% error in the measurements. The error from the mode pulling effect at 6328Å and 11523Å was less than 2%.

The applications of a three-wavelength system are twofold. First, three unknowns could be readily measured. Secondly, if only two unknowns are important, information at a third wavelength would provide a convenient check.

The next category listed for future work was the continuation

of studies in argon. For example, a three-wavelength system could be used to check the consistency of the present results. Also, if the system bandwidth can be significantly increased, measurements at higher discharge currents will be possible. At high enough electron densities, this technique could conceivably be used to study the effect of excited ions on the refractive index. A partial energy level diagram for AII showing the ionic metastable levels is given in Appendix I.

The last area mentioned for future work was the extension of these techniques to other gases and even gas mixtures. Gases which have not been studied with this system include neon, xenon, krypton, nitrogen, and carbon dioxide. Partial energy level diagrams for neon, xenon, and krypton showing the atomic metastable levels are given in Appendix I. In order to study neon, of course, one would not use a helium-neon laser system. An alternative might be to use argon lasers. However, it should be noted that there are strong neon transitions within 1Å of the lowest threshold argon laser lines (4880Å and 5145Å). The drawback to studying xenon and krypton is the scarcity of values for their oscillator strengths.

Finally, this interferometer approach could be used for investigating gas mixtures. For example, information obtained at the 11523Å wavelength could be used to study the destruction of the helium triplet metastable level in helium-mercury, helium-argon or helium-carbon dioxide discharges.

APPENDIX I

MISCELLANEOUS INFORMATION ON AII, NeI, KrI, AND XeI

In Section 2.4, certain energy levels of the argon ion were listed. The nomenclature which was used for designating these levels is known as the LS coupling notation. In quantum number form, this notation is written as $n\ell\ (^{2S+1}L_J)$, where n applies to the single jumping electron and $(^{2S+1}L_J)$ relates to the whole atom. Recall that "n" is the principal quantum number, ℓ is the single electron's orbital angular momentum, 2S + 1 is the multiplicity with S being the total atom's spin, L is the total orbital angular momentum quantum number, and $J = |L + S|, |L + S| - 1, \ldots. |L - S|$, is the total angular momentum quantum number. The superscript "o" which in some cases is associated with L indicates a level with odd parity. The lack of a superscript "o" designates an even parity level. The prime attached to the ℓ value of the excited electrons for certain levels, implies that the core or unexcited part of the atom has a quantum number $J_c = \frac{1}{2}$. The lack of a prime corresponds to $J_c = \frac{3}{2}$.

With regard to Chapter V, the possibility of investigating additional gases was mentioned. Since experience with argon, helium, and mercury discharges has revealed the importance of metastable index of refraction contributions, the preliminary aspects of extending this research to other gases will involve knowing which levels

in these new gases are metastable. Appropriate information for ionized argon, neutral neon, neutral krypton, and neutral xenon has been obtained as an outgrowth of a literature review which was done for the present argon study.

An energy-level diagram for the argon ion is given in Figure A1.1. For the purpose of keeping the diagram readable, only those levels having a core with $J_c = \frac{3}{2}$ were included. The diagonal lines in this diagram indicate that there are numerous levels which have the specified type of electron. For example, there are actually five individual levels having 4s electrons which lie within the cross-hatched region labelled "4s."

The AII metastable levels shown in Figure A1.1 are the $3d^2F_{7/2}$, $3d^4F_{7/2,\ 9/2}$, and $3d^4D_{7/2}$ levels. In addition, the levels $3d'^2G_{7/2,\ 9/2}$ and $3d'^2F_{7/2}$ are metastable. They are not listed in Figure A1.1 since the core atom associated with these excited states has an angular momentum $J_c = \frac{1}{2}$.

Energy level diagrams for the neon, krypton, and xenon atoms are given in Figures A1.2, A1.3, and A1.4, respectively. In neutral neon, the levels 3s(J = 2) and 3s(J = 0) are stable against dipole radiation to the ground state and hence are metastable. Since all four of the 3s levels are closely spaced, moreover, the two 3s(J = 1) levels might readily have population densities comparable to the true metastable states.

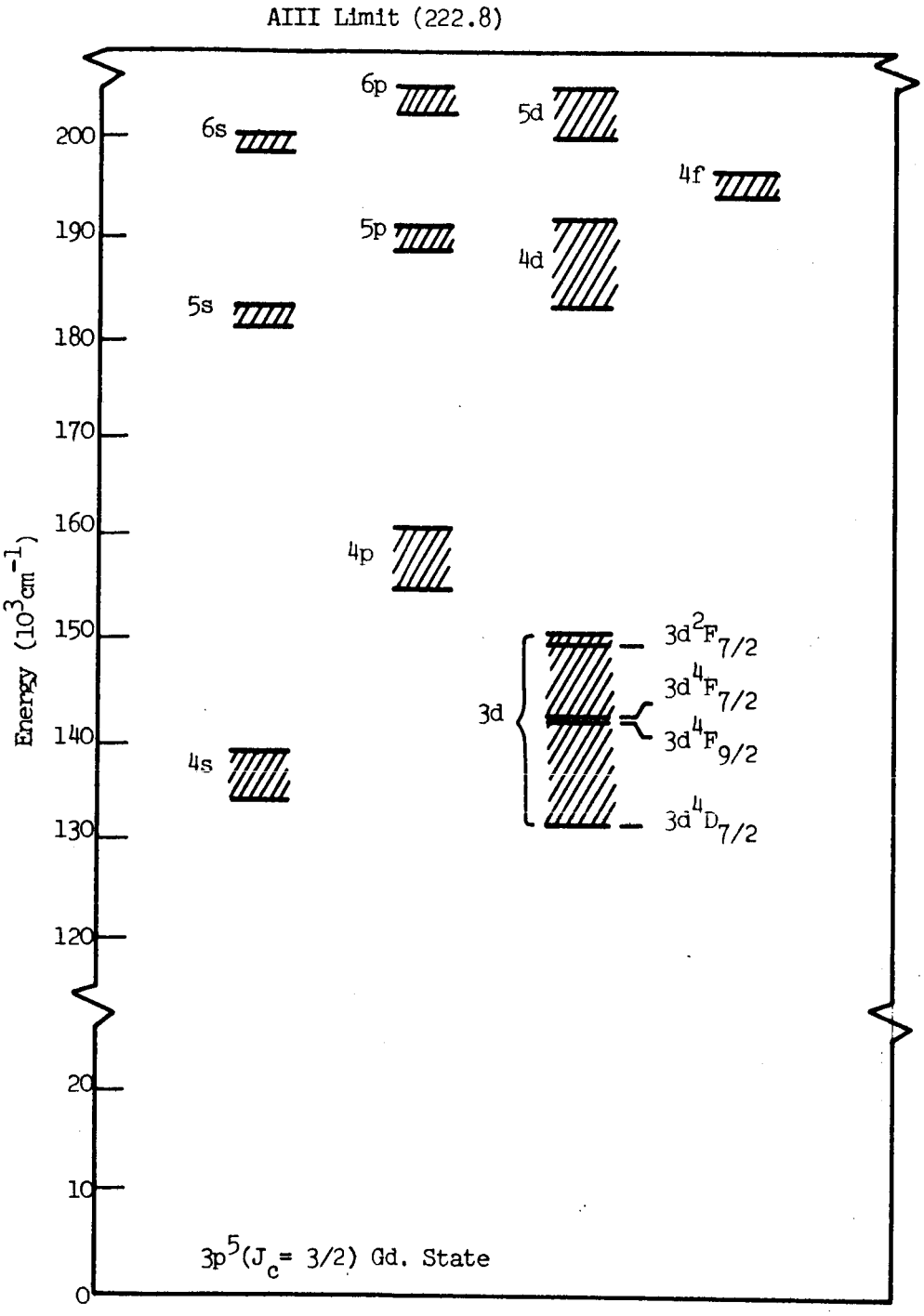

Figure A1.1 Energy-Level Diagram for the Argon Ion (Core: $3s^2\ 3p^5\ {}^2P^o_{3/2}$).

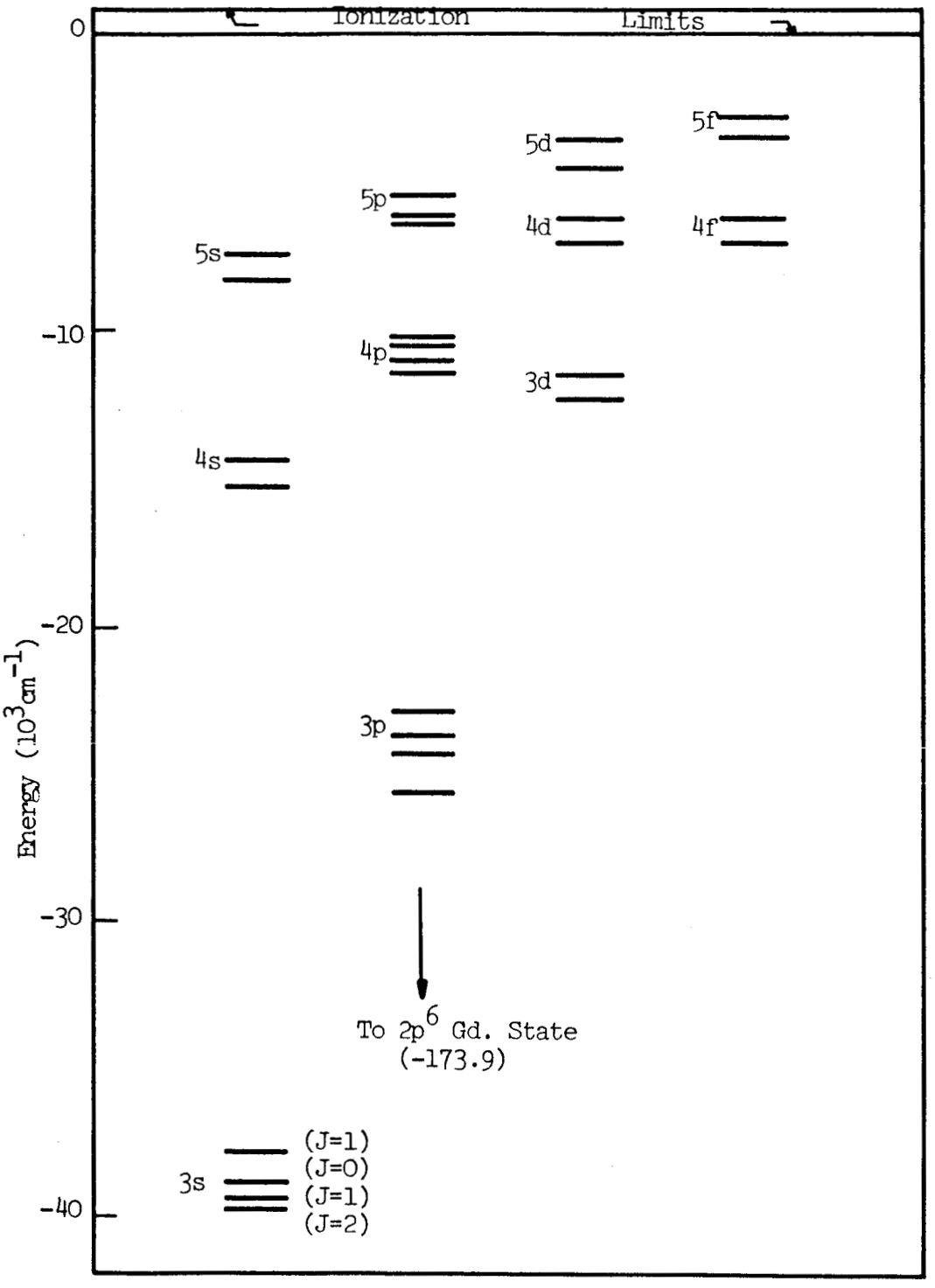

Figure A1.2 Energy-Level Diagram for the Neon Atom.

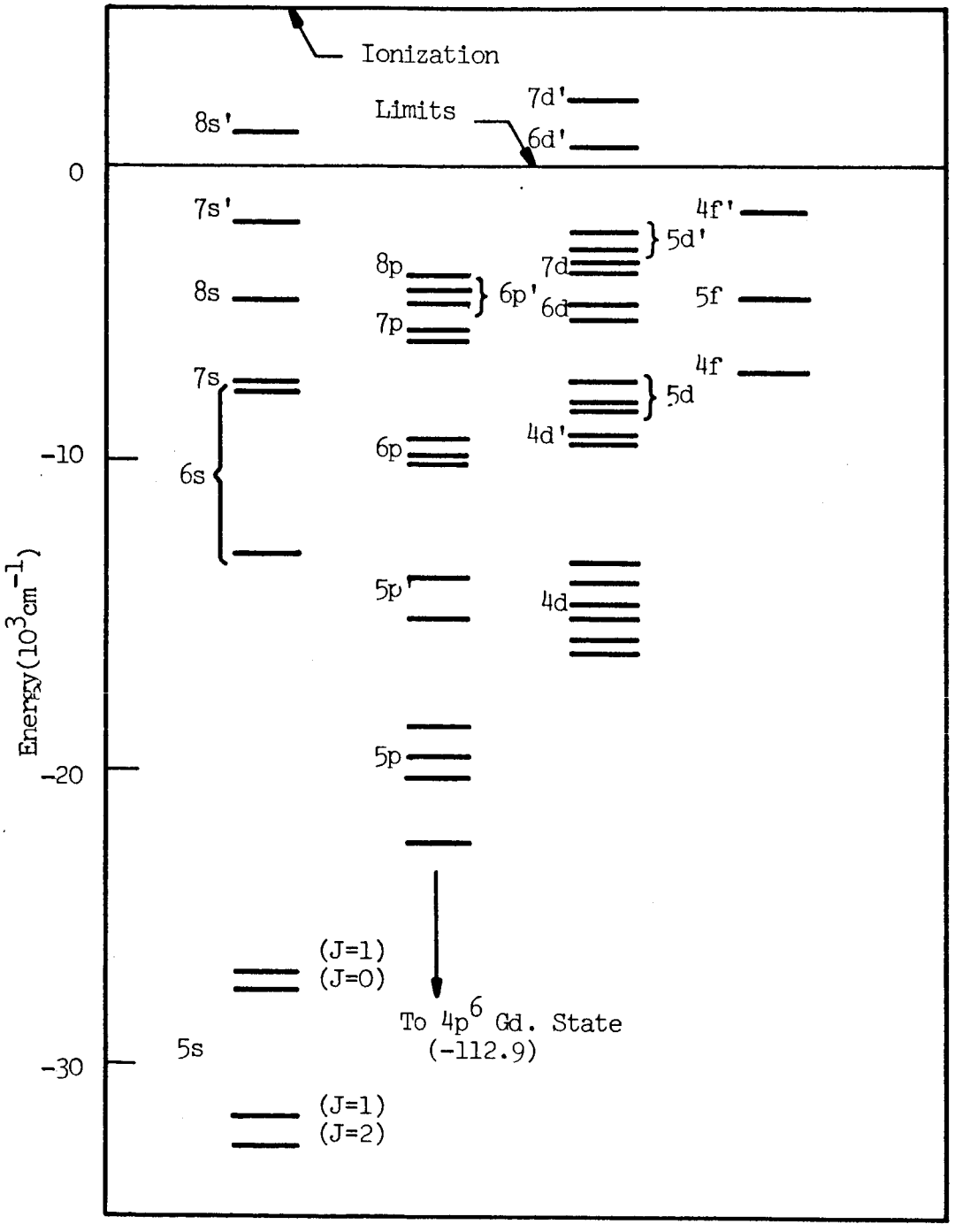

Figure A1.3 Energy-Level Diagram for the Krypton Atom.

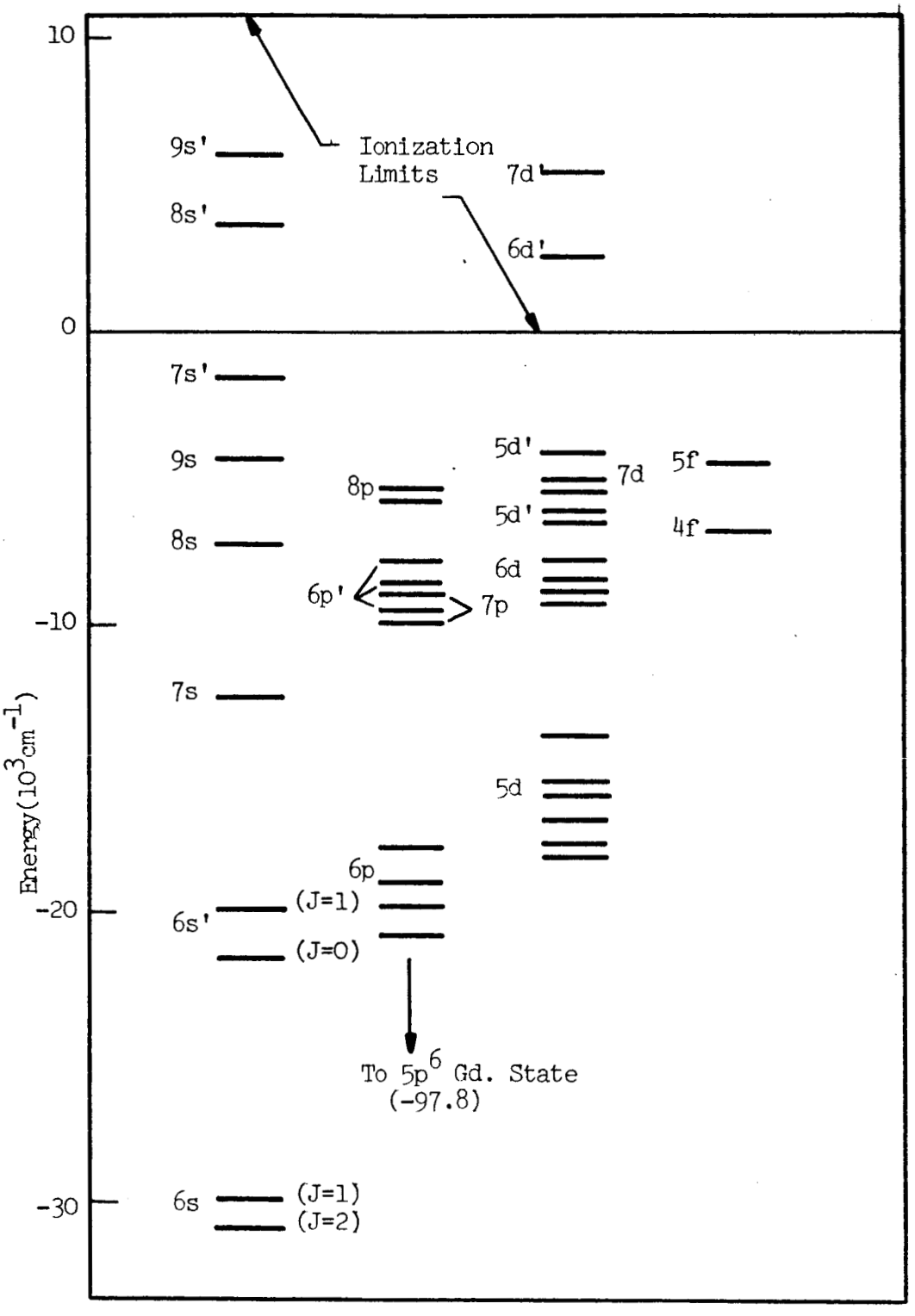

Figure A1.4 Energy-Level Diagram for the Xenon Atom

Krypton also has two levels which are stable against dipole radiation. They are the 5s(J = 2) and 5s(J = 0) states. Again, the proximity of the 5s(J = 0) level to the higher lying 5s(J = 1) level leads one to expect a considerable population of atoms in the 5s(J = 1) state. A similar condition exists for the lower lying pair of 5s levels, whereby the density of the other 5s(J = 1) excited state would be enhanced by the 5s(J = 2) metastable.

Finally, the situation for xenon is analogous to that for krypton. The 6s(J = 2) and 6s'(J = 0) levels are metastable, whereas the 6s(J = 1) and 6s'(J = 1) levels are effectively metastable.

The degree to which the radiating "s" levels of the rare gases are effectively metastable depends in part on whether the resonance radiation from these levels is trapped. Since, the importance of resonance trapping depends on the particular discharge conditions, a further evaluation of this effect is not appropriate here.

When the index of refraction contribution due to metastables is calculated for a given gaseous discharge, it is necessary to know the values of the absorption oscillator strengths (or equivalently the transition probabilities) for transitions involving the various metastable levels. For AII, oscillator strengths are given in Griem [42] or the many references listed in the National Bureau of Standards Bibliography on Atomic Transition Probabilities.[43] Oscillator strengths for transitions in neon have been treated

extensively. A "best value" listing has recently been published by the National Bureau of Standards.[44] The atomic parameters for krypton and xenon are less widely available. An up-to-date reference list is given in the National Bureau of Standards bibliography on transition probabilities.[45]

APPENDIX II

ELECTRONIC CIRCUITS

The schematic diagram for the SCR inverter circuit is given in Figure A2.1. This device is capable of handling currents as large as 30 amperes r.m.s. The duty cycle of the square-wave current waveform is variable since the "on" and "off" times are both independently adjustable from 4ms to 40 ms.

The operation of this unit is as follows. Let switch S be initially open. Once the 30v supply is turned on, the 0.47 μfd capacitor associated with unijunction transistor #1 (UJT #1) charges. When sufficiently charged, this capacitor "fires" UJT #1. The resulting pulse trigers SCR #1 and allows current to flow from the main 800v supply mostly through the 200 ohm "dummy" load. Also, assuming that a small keep alive current is maintained through the laser, the commutating capacitor C_c charges to some 600 volts, i.e. 800 volts minus the discharge tube operating voltage ($\sim$ 200 volts). If switch S is now closed, UJT #2 fires and delivers a pulse to trigger SCR #2. Once SCR #2 conducts, the side of capacitor C_c which was at +600 volts is suddenly pulled to near 0 volts. The result is that C_c then attempts to drive the anode side of SCR #1 to -600 volts. Although diode D2 keeps this voltage near ground potential, the appearance of a negative-going voltage turns SCR #1 off.

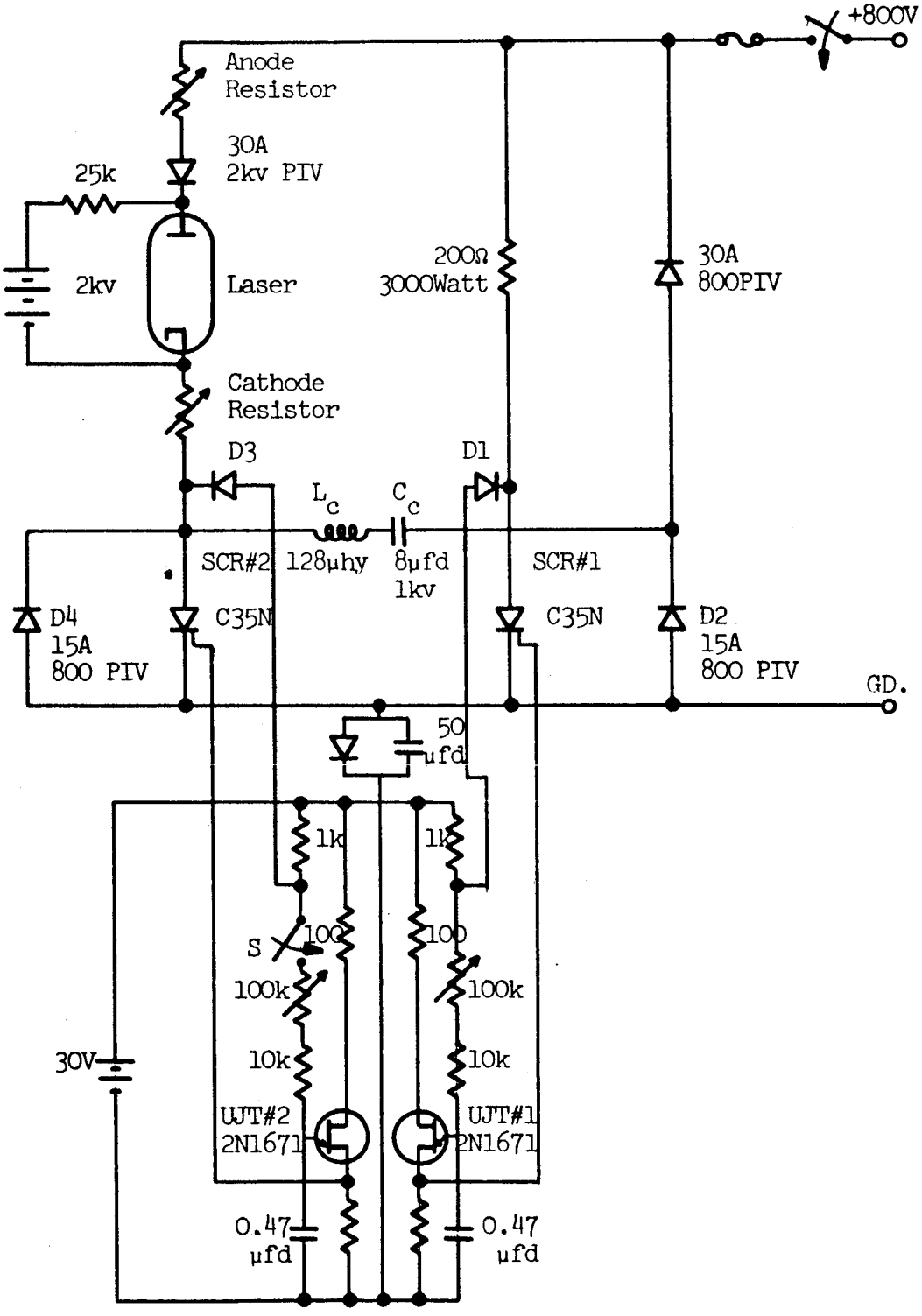

Figure A2.1 SCR Inverter Circuit

Thus, with SCR #1 off, diode D1 is back-biased and UJT #1 can again fire. Meanwhile C_c is once more charged, this time to 800 volts through the 200 Ω, 3000 Watt resistor. Hence when UJT #1 does fire and triggers SCR # 1 to conduct, C_c tries to drive the anode of SCR #2 negative and therefore turns this SCR off. Diode D4 assures that the cathode side of the laser never really goes negative and consequently removes the danger of drawing a disasterously large current through the discharge. With SCR #2 off again, diode D3 is back-biased and UJT #2 can re-fire. The process repeats itself until switch S is opened.

In addition to the SCR inverter, a single-shot square-wave pulser was used for regulating the current through the experimental argon discharge tubes. The schematic diagram for this circuit is given in Figure A2.2. Basically, this device utilizes two 2D21 thyratron tubes for controlling a capacitor discharge across the plasma tube.

Finally, a circuit designed for precisely turning off the discharge is given in Figure A2.3. This circuit was used in determining the magnitude of the beat frequency shift associated with the small keep alive current. The principal feature of this device is that it is controlled by the gate voltage from an oscilloscope. That is, with the scope in its single-sweep mode, the turn-off event is initiated by pressing the scope's reset button. The first part of the sweep, therefore, corresponds to the current "on" condition.

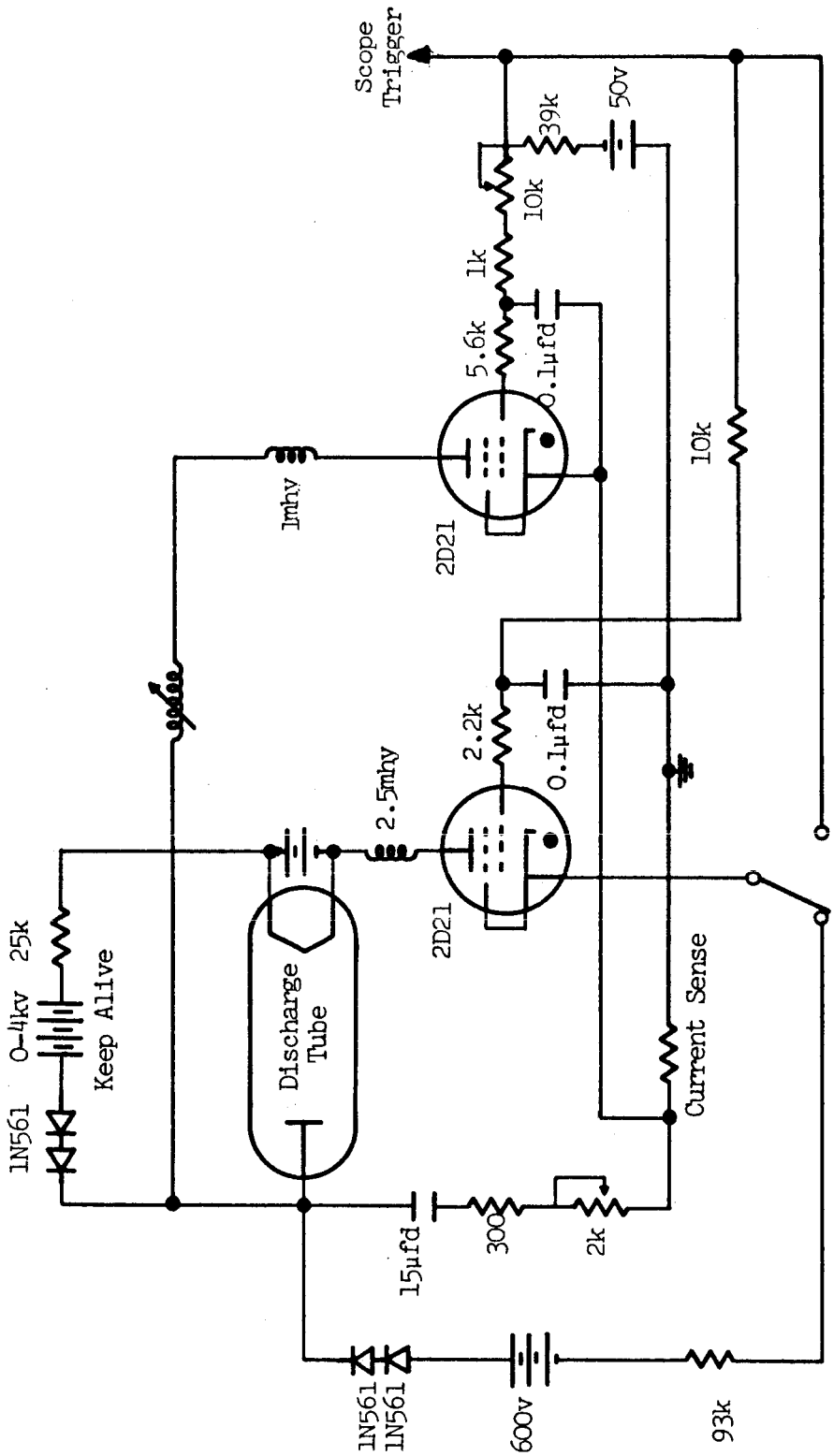

Figure A2.2 Square-Wave Current Pulser

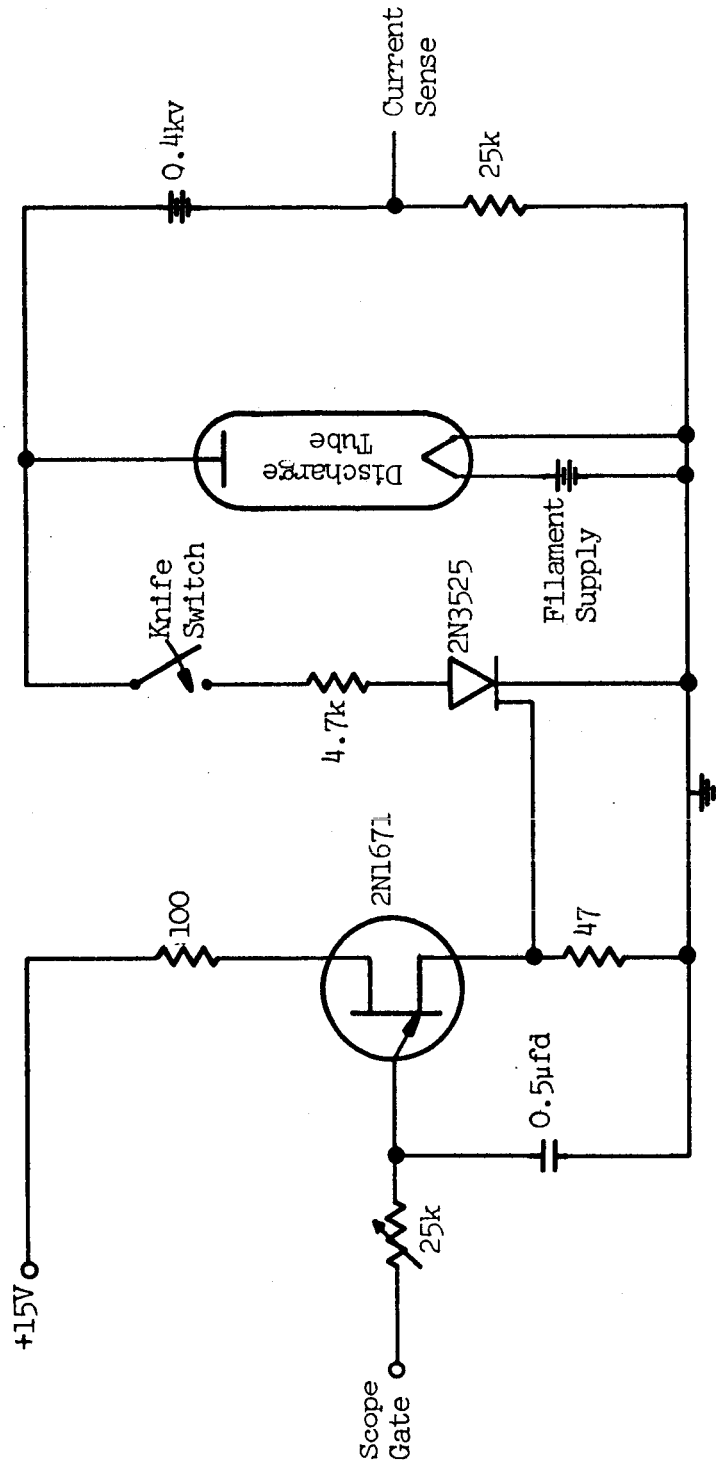

Figure A2.3 Turn-Off Circuit

Following a variable length delay, the SCR is triggered and conducts the current away from the discharge tube. Hence the last part of the scope sweep is for the current "off" condition. The knife switch is used for protecting the SCR when the tube is re-lighted.

LIST OF REFERENCES

1. W. B. Johnson, IEEE Trans Antennas Propagation, AP-15, 152 (1967).

2. W. B. Johnson, A. B. Larsen, and T. P. Sosnowski, Proceedings of the Seventh International Conference on Phenomena in Ionized Gases, Belgrade, 1966.

3. E. F. Labuda, C. E. Webb, R. C. Miller, and E. I. Gordon, "A Study of Capillary Discharges in Noble Gases at High Current Densities," unpublished report from Bell Telephone Laboratories, Incorporated, Murray Hill, New Jersey.

4. W. R. Bennett, Jr., Appl. Phys. Letters 4, 180 (1964).

5. W. Demtroder, Phys. Letters 22, 436 (1966).

6. G. Birnbaum, Optical Masers, Academic Press, New York, 1964, p. 31.

7. A. B. Larsen, Ph. D. Thesis, Case Institute of Technology, 1966, p. 15.

8. W. B. Thompson, An Introduction to Plasma Physics, Pergamon Press, Oxford, 1962, p. 11.

9. G. A. Cook, Argon, Helium and the Rare Gases, Vol. I, Interscience, New York 1961, p. 238.

10. A. C. Mitchell and M. W. Zemansky, Resonance Radiation and Excited Atoms, University Press, Cambridge, 1934, p. 140.

11. M. A. Uman, Introduction to Plasma Physics, McGraw-Hill, New York, 1964, p. 96.

12. G. R. Harrison, (ed.), M.I.T. Wavelength Tables, Wiley, New York, 1939.

13. G. E. Moore, A Multiplet Table of Astrophysical Interest (revised edition), New Jersey, 1945, p. 21-23.

14. H. E. White, Introduction to Atomic Spectra, McGraw-Hill, New York, 1934, p. 274.

15. Pointed out by Dr. R. C. Miller of Bell Telephone Laboratories, Murray Hill, New Jersey, in a private communication.

16. Ibid.

17. R. H. Garstang and J. Van Blerkom, J. Opt. Soc. Amer. 55, 1054 (1965).

18. B. D. Adcock and W. E. Plumtree, J. Quant. Spectrosc. Radiat. Transfer 4, 29 (1964).

19. H. R. Griem, Plasma Spectroscopy, McGraw-Hill, New York, 1964, p. 176.

20. Pointed out by Dr. Bentley Barnes of General Electric in a personal conversation.

21. S. N. Levine, Quantum Physics of Electronics, Macmillan, New York, 1965, p. 122.

22. Griem, op. cit., p. 438.

23. B. Edlen, Reports on Progress in Physics, Vol. XXVI, 1963, p. 181.

24. A. B. Larsen, Ph. D. Thesis, Case Institute of Technology (1966).

25. G. D. Boyd and J. P. Gordon, Bell Syst. Tech. J. 41, 489 (1961).

26. G. D. Boyd and H. Kogelnik, Bell Syst. Tech. J. 41, 1347 (1962).

27. B. M. Oliver, Proc. Inst. Radio Engrs. 49 1960 (1961).

28. Ibid.

29. E. I. Gordon and E. F. Labuda, Bell Syst.Tech. J. 43 1827 (1964).

30. U. Ascoli-Bartoli, A. DeAngelis, S. Martellucci, Nuovo Cimento 18 1116 (1960).

31. J. B. Gerardo, J. T. Verdeyen, and M. A. Gusinow, J. Appl. Phys. 36 3526 (1965).

32. A. B. Larsen, Ph.D. Thesis, Case Institute of Technology, 1966, p. 78.

33. J. D. Cobine, Gaseous Conductors, McGraw-Hill, New York, 1941, p.43.

34. S.C. Brown, Basic Data of Plasma Physics, 1966, M.I.T., Cambridge, 1967, p.22.

35. E.F. Labuda, et al., "A Study of Capillary Discharges in Noble Gases At High Current Densities," unpublished report.

36. Ibid.

37. A. V. Phelps and J. P. Molnar, Phys. Rev. 89 1202 (1953).

38. K. G. Hernqvist and J.R. Fendley, Jr., IEEE J. Quan. Elect. QE-3 66 (1967).

39. Ibid. p. 67.

40. E. F. Labuda, et al., "A Study of Capillary Discharges in Noble Gases At High Current Densities," unpublished report.

41. Brown, op. cit., p. 11.

42. Griem, op. cit., p. 414.

43. B. M. Glennon and W. L. Wiese, Bibliography On Atomic Transition Probabilities, National Bureau of Standards Miscellaneous Publication 278, 1966.

44. National Bureau of Standards Monograph, Atomic Transition Probabilities NSRDS - NBS - 4 (1966).

45. B. M. Glennon, op. cit.